Engineering Fracture Mechanics 308 (2024) 110338

Contents lists available at ScienceDirect

Engineering Fracture Mechanics

journal homepage: www.elsevier.com/locate/engfracmech

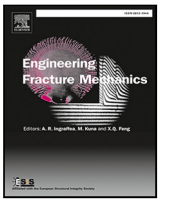

Static assessment of flawed notched components manufactured by L-PBF in AlSi10Mg: Experiments, computational approaches, a simplified method

G. Minerva [a], I. Pozzoni [a], F. Zarei [a], S. Beretta [a,b,*]

[a] Politecnico di Milano, Department of Mechanical Engineering, via La Masa 1, 20156, Milano, Italy
[b] Auburn University, National Center for Additive Manufacturing Excellence (NCAME), Auburn, AL 36849, United States of America

ARTICLE INFO

Keywords:
Laser Powder Bed Fusion
AlSi10Mg
Static fracture assessment
Mechanical properties
Fracture toughness

ABSTRACT

The assessment of parts produced by Additive Manufacturing against static loading requires to account for several factors, such as process-induced defects and heterogeneous microstructure, which cause dependence of the material properties on the building position. In this work, a comprehensive approach to the static assessment of AlSi10Mg notched test articles manufactured by Laser Powder Bed Fusion (L-PBF) is presented. A test campaign on thin notched AlSi10Mg parts manufactured by L-PBF confirms that, despite the quasi-brittle tensile behaviour, an assessment based on elastic–plastic fracture mechanics parameters is needed to correctly predict the experimental failures. Predictions based on Failure Assessment Diagram and Theory of Critical Distances are then compared with experimental results. A simplified Imaginary Crack Model method, based on the concepts of Fictitious Crack Length, resulted to be quite precise and simple to apply.

1. Introduction

Laser Powder Bed Fusion (L-PBF) allows the production of components with complex geometries derived from topological optimization, which is particularly relevant for the aerospace industry [1,2]. However, the freedom of design comes at the price of increased complexity in the assessment of components. In fact, L-PBFed components are characterized by heterogeneous microstructure, the inherent presence of anomalies, an orientation-dependent surface quality, and residual stresses. Among these, the inherent presence of anomalies might be particularly critical. Different types of L-PBF anomalies with a large range of dimensions have been extensively described in the literature, from small gas entrapped porosity to lack-of-fusion and keyhole porosity of the order of a few tenths of millimetre [3–7]. Anomalies might play a particularly important role for the unstable fracture of space components, which are mainly designed for static loads [8] and for which active standards require the definition of a critical defect size [9]. The identification of a fracture-based static assessment suitable for the characteristics of L-PBFed components is thus of paramount importance.

Several fracture-based tools are already employed for the static assessment of components in the presence of anomalies. The preference of one method over the others needs to be evaluated based on the required accuracy and on the ease of use for topologically optimized components with several stress concentration features, and in relation to the material. The AlSi10Mg employed in this study has been extensively investigated in the literature [10]. The authors showed in a previous work [11] that,

* Corresponding author at: Politecnico di Milano, Department of Mechanical Engineering, via La Masa 1, 20156, Milano, Italy.
E-mail address: stefano.beretta@polimi.it (S. Beretta).

https://doi.org/10.1016/j.engfracmech.2024.110338
Received 19 March 2024; Received in revised form 12 July 2024; Accepted 26 July 2024
Available online 7 August 2024

Nomenclature

Abbreviations

3PB	Three-point bending
AB	As-built
AM	Additive Manufacturing
B	Bending notched specimen
B3D	Bending notched specimen with three-dimensional defect
CDF	Crack Driving Force
CT	Compact Tension
DA	Direct ageing
EBSD	Electron Back-Scattered Diffraction
EDM	Electro-Discharge Machining
EPFM	Elastic–Plastic Fracture Mechanics
FAD	Failure Assessment Diagram
FCL	Fictitious Crack Length
FE	Finite Element
FPZ	Fracture Process Zone
HV	Vickers Hardness
ICM	Imaginary Crack Model
IPF	Inverse Pole Figure
L-PBF	Laser Powder Bed Fusion
LEFM	Linear Elastic Fracture Mechanics
SEM	Scanning Electron Microscope
SIF	Stress Intensity Factor
SR	Stress relieving
T	Tensile notched specimen
TCD	Theory of Critical Distances

Symbols

$\bar{K}_r$	Ratio between SIF and $K_{I,c}$ of FAD assessment point
$\bar{L}_r$	Ligament yielding of FAD assessment point
Δa	Crack advancement
ΔK	SIF range
ν	Poisson's ratio
σ	Engineering stress
σ_0	Material inherent strength of TCD model
σ_{flow}	Flow stress
σ_{ref}	Reference stress of FAD formulation
$\sigma_{rem,FE}$	Remote stress applied in FE simulations
σ_{rem}	Remote stress of FAD formulation
σ^*_{rem}	Remote stress of collapse of FAD formulation
σ_{VM}	Von Mises equivalent stress
$\sqrt{area}$	Square root of the projected area of the crack perpendicular to the opening stress
ε	Engineering strain
ε_f	Failure strain
ε_{ref}	Reference strain of FAD formulation
a	Crack depth or length
a^*_∞	Material parameter of Hu and Liang ICM
a_0	Fictitious crack length
a_{eq}	Equivalent crack length of B3D specimens in the FCL model

B	Specimen thickness
c	Crack half-width
D	Nominal length of the induced defects
E	Young modulus
F	Tensile load
F_y^*	First-yield tensile load of the net section without the notch
F_0	Tensile collapse load of FAD formulation
F_{CDF}	Tensile failure load predicted with computational CDF
F_{EXP}	Experimental tensile failure load
F_{FAD}	Tensile failure load predicted with FAD
F_{FCL}	Tensile failure load predicted with FCL
$F_{flow,crack}$	Local plastic collapse tensile load at flow stress accounting for section partialization due to the crack
F_{flow}	Local plastic collapse tensile load at flow stress
F_{TCD}	Tensile failure load predicted with TCD
h	Height of the induced defects
h^*	Hatch distance
J	J-integral
J_{el}	J-integral obtained with linear elastic material properties
$J_{I,c}$	Critical material fracture toughness expressed in terms of J-integral
K	SIF
K_t	Stress concentration factor
$K_{I,c}$	Critical material fracture toughness expressed in terms of SIF
K_{rs}	SIF due to residual stresses
K_r	Ratio between SIF and $K_{I,c}$
L	Material critical distance of TCD model
L_r	Ligament yielding
M	Bending moment
M_0	Bending moment of collapse of FAD formulation
M_{CDF}	Failure bending moment predicted with computational CDF
M_{EXP}	Experimental failure bending moment
M_{FAD}	Failure bending moment predicted with FAD
M_{FCL}	Failure bending moment predicted with FCL
$M_{flow,crack}$	Bending moment of local plastic collapse at flow stress accounting for section partialization due to the crack
M_{flow}	Bending moment of local plastic collapse at flow stress
$M_{I,p}^*$	First-yield bending moment of the net section without the notch
M_{TCD}	Failure bending moment predicted with TCD
n	Ramberg–Osgood exponent
P	Generic load of FAD formulation
P_L	Laser beam power
P_0	Generic collapse load of FAD formulation
P_{EXP}	Generic experimental failure load
$P_{prediction}$	Generic failure load predicted with the investigated methods
R	Load ratio
R_m	Ultimate Tensile Stress
$R_{p,0.2\%}$	Yield Strength corresponding to 0.2% plastic strain
t	Layer thickness
V	Weight factor for residual stresses in the FAD formulation
v	Scan speed
W	Specimen width at the notch root
W_{rem}	Specimen remote width
Y	Boundary (or finite width) correction factor

despite the quasi-brittle (or micro-ductile) behaviour shown by AlSi10Mg in its as-built (AB) state (i.e. without any heat treatment), Elastic–Plastic Fracture Mechanics (EPFM) was needed to accurately describe failures of thin flawed benchmark specimens subjected

to tensile or bending loads. In particular, computational Crack Driving Force (CDF) and the Failure Assessment Diagram (FAD) were successfully employed to predict the static failure of the benchmark specimens object of the study.

The relevant CDF parameter for components loaded below one third of the yield strength is the Stress Intensity Factor (SIF) K [12], which can be computed with dedicated Finite Element (FE) analyses or estimated analytically using solutions from compendia [13–15]. For higher levels of stress, different CDF parameters, such as the J-integral, are needed. However, computational CDF analyses based on the J-integral are typically complex and time consuming. To avoid this, a simplified approach based on the FAD was developed in the 1970s for power generation applications [16]. The FAD procedure provides an approximation of elastic–plastic CDF by correcting linear elastic CDF in a fully analytical framework. Notably, the FAD found wide industrial application in the aerospace, civil, offshore and chemical sectors [17–19], also thanks to the formalization provided by dedicated standards [15,20,21]. Of particular relevance is the successful application of the FAD for welds [22], for which manufacturing anomalies are similar to those induced by the L-PBF process [23,24].

A second possibility for the static assessment of components in presence of flaws is the Theory of Critical Distances (TCD). The TCD dates back to the late 1950s with Neuber's and Peterson's independent studies on fatigue failures in the presence of notches. Many similar approaches were discovered in the following years and the TCD was then formalized in the current framework by Taylor in the early 2000s. Taylor describes the TCD as a group of theories for the prediction of failure based on the evaluation of the linear elastic stress distribution arising from a critical feature (i.e. a notch or a crack). In particular, failure is predicted when the equivalent stress computed from the stress distribution over a material-dependent critical distance L is equal to the so-called material inherent strength σ_0 [25]. For brittle failures, material inherent strength σ_0 is equal to the ultimate tensile strength (UTS) and the critical distance L depends only on UTS and plane strain fracture toughness $K_{I,c}$. However, when a limited amount of plastic deformation occurs before failure, σ_0 and L need to be obtained from dedicated experiments on notched components with stress concentration features that induce very different states of stress, i.e. a blunt notch and a sharp notch [26,27]. The success of the TCD for industrial applications [28–30] can be related to the possibility of employing a simple linear elastic FE analysis to assess a component with a relatively simple post-processing of the stress distributions near the stress concentration features. Nevertheless, if failure due to unstable fracture of flaws is to be investigated, then multiple FE analyses need to be carried out to identify the critical size of the crack, given a certain location, orientation and shape.

To avoid the explicit modelling of cracks in FE analyses it is possible to employ an Imaginary Crack Method (ICM), which assumes the presence of an imaginary crack with a material-dependent size for which the critical load can be computed by applying Linear Elastic Fracture Mechanics (LEFM) [28]. For what concerns static assessment, many similar approaches have been proposed in the literature. The first formulation was given by Waddoups et al. [31], who used an ICM to describe the static failure of flawed laminated composite materials. For the composite materials investigated by Waddoups et al. a damage zone was observed at the notch root prior to failure, which size was hypothesized to be in relation with the imaginary crack. In fact, a physical interpretation of ICM has been suggested by using the Barenblatt–Dugdale model. Barenblatt's fictitious crack model describes the conditions for crack propagation using energy considerations on the crack tip for brittle materials [32]. On the other hand, Dugdale's model describes crack-tip yielding for elastic-perfectly plastic materials with a fictitiously increased crack length [33]. Barenblatt–Dugdale models, first developed by Hillerborg [34], allow to describe the fracture process zone (FPZ) by means of energetic consideration on crack propagation. The interesting point is that TCD, ICM and FPZ models have been proven to produce the exact same formulation, at least for simple 2D cases that can be treated analytically [28]. Therefore, despite the significantly different approaches, Finite Fracture Mechanics models, such as the ICM, and Continuum Mechanics models, such as the Barenblatt–Dugdale model and the TCD, lead to an analogous description of critical loads. This may very well be related to the fact that all the aforementioned models are ultimately referring to the same Type II size effect formulation described by Bažant, which links two asymptotic limits: a stress-based criterion and an energy-based criterion [35], with the link between the two asymptotes providing an approximation of EPFM [36].

To investigate the capabilities of the aforementioned methods to predict failures of L-PBFed components with complex geometrical features, we adopted four notched benchmark fracture specimen geometries, covering two different stress concentrations, U and V notches, and two loading conditions, tension and bending. The benchmark specimens were printed alongside tensile and fracture toughness standard specimens for material characterization. Failure loads were then predicted with computational CDF analyses, FAD, TCD and a modified ICM method.

The structure of this paper is as follows: Section 2 describes the specimen geometries and the experimental setup, Section 3 reports material properties as well as the results of the benchmark specimens' static fracture tests. Prediction of failure loads of all benchmark specimens were carried out with computational CDF analyses, reported in Section 4. Predictions of the failure loads of thin notched tensile and bending specimens were also carried out with different methods: Section 5 introduces the FAD procedure and shows its application with computational and analytical formulations, while the TCD approach is described in Section 6. Section 7 provides a critical discussion on the application of the different methods to the notched tensile and bending specimens and a modification to an ICM analytical method is presented. Finally, conclusions are summarized in Section 8.

2. Experimental plan

AlSi10Mg material characterization specimens and notched benchmark specimens were manufactured using an EOS M 400 system equipped with four 400 W Yttrium fibre lasers working in parallel in a build chamber that measures 400 × 400 × 400 mm^3. The printing parameters were the ones suggested by equipment manufacturer: beam power P_L = 370 W, hatch distance h^* = 0.19 mm and scan speed v = 1300 mm/s. The layer thickness was t = 30 μm and the resulting energy density was 49.93 J/mm^3. During printing, the building platform was heated to a temperature of 165 °C. The powder particles were sampled and prepared

Table 1
Chemical composition (wt%) of AlSi10Mg powder.

Al	Si	Fe	Cu	Mn	Mg	Ni	Zn	Pb	Sn	Ti	Others
Balance	9.3	0.15	<0.01	<0.01	0.32	<0.01	<0.01	<0.01	<0.01	0.01	<0.15

according to ASTM B215 [37]. AlSi10Mg powder size distribution analysis was carried out by means of laser diffraction, resulting in a particle size distribution with D_{10} = 26 μm, D_{50} = 47 μm and D_{90} = 76 μm. Powder particles chemistry analysis was carried out by Inductively Coupled Plasma - Optical Emission Spectroscopy and allowed to obtain the composition reported in Table 1. The specimens' minimum relative density was 99.7%, measured by metallography on polished sections according to ASTM F3637 [38].

The specimen geometries are shown in Fig. 1. All the manufactured specimens did not undergo any post-processing operation (e.g. heat treatments) and were tested in the AB condition.

2.1. Tensile and fracture toughness tests

The specimen geometries depicted in Fig. 1(a) aimed to characterize the tensile behaviour and the fracture toughness. The tensile tests were performed according to the ASTM E8 standard [39] on an MTS Alliance RT 100 load frame, equipped with a 100 kN load cell using cylindrical and flat tensile specimens having a relevant dimension (i.e.: nominal diameter/thickness) of 6 mm. The strain was measured with an MTS extensometer with 8 mm gauge length. The cylindrical specimens were manufactured in four build jobs, J1, J2, J3 and J4, on the base plate, while the flat specimens were obtained by Electro-Discharge Machining (EDM) on the top part of thin plates manufactured with the full print height (160 mm) in build Job J2 (Fig. 1(c)).

The fracture toughness tests were conducted according to the ASTM E1820 standard [40] by adopting the resistance curve (R-curve) method on Compact Tension (CT) specimens. CT specimens were manufactured in four build jobs, J1 to J4, both on the base plate and with the same crack plane as the notched benchmark specimens (Fig. 1(c)). The fracture toughness tests were carried out on an MTS 810 machine equipped with a 10 kN load cell and an MTS clip-on gauge with a nominal length of 5 mm. Before the tests, all specimens were subjected to fatigue load cycling with decreasing SIF range ΔK at constant load ratio $R = 0.1$ to produce fatigue cracks with a length of approximately 1.5 mm. To avoid tunnelling of the crack during the test, side-grooving was performed on the specimens' flanks with a depth of 1.25 mm per side. After the tests conducted in load control, images of the fracture surfaces were captured by means of a 2 Megapixel Allied Vision Manta CCD camera equipped with a lens system produced by Navitar. The fractographies, reported in Fig. A.1 in Appendix A, were used to measure the pre-crack and the final crack lengths after specimens' failure.

All material characterization tests were carried out in air at room temperature. Two sets of material properties were thus obtained: Base material properties for cylindrical tensile specimens and CT specimens manufactured on the base plate and High material properties for flat tensile specimens and CT specimens manufactured with the same crack plane as the benchmark specimens, with a distance of 80 mm from the build plate.

2.2. Tests on notched benchmark specimens

Notched benchmark specimens were produced together with material characterization specimens in four build jobs, J1 to J4. Different geometries were included into the experimental phase, simulating two different stress localization: a U notch (N1) with root radius equal to 9 mm and a V notch (N2) with root radius equal to 4 mm, both having a notch depth of 9 mm, as shown in Fig. 1(b). Two notches were introduced in thin notched tensile (T) specimens to guarantee symmetry of the load, while one notch was introduced in thin notched bending (B) specimens and in thick notched bending specimens with 3D defects (B3D). T and B benchmark specimens had a thickness of 6 mm, while the thickness of B3D benchmark specimens was 12 mm.

2.2.1. Flaws and pre-cracks

Through thickness defects were introduced at the notch root of T and B benchmark specimens (Fig. 2(a)) either by wire EDM (Fig. 2(b,d)) or during the specimen manufacturing (Fig. 2(c,e)). The defects had different nominal length D, from 0.25 mm to 2 mm: three defect lengths were realized by EDM (D0.25, D1 and D2) and three defect lengths were obtained during the printing phase (D0.5, D1 and D2). For B3D notched specimens, two types of 3D defects were introduced at the notch root, as shown in Fig. 3(a): semicircular defects with radius equal to 2 mm and rectangular defects having a width of 8 mm and a depth of 1 mm. Fig. 3(b) shows a semicircular defect obtained by plunge EDM (DS_E), while a semicircular defect obtained during the printing phase (DS_P) is shown in Fig. 3(d). Similarly, rectangular defects realized by plunge EDM (DR_E) and during printing (DR_P) are shown in Fig. 3(c) and (e), respectively. For T and B benchmark specimens, the height h of the defects obtained by wire EDM was of 0.36 mm, while 3D defects obtained by plunge EDM in B3D benchmark specimens had a height h of 1 mm. All printed defects were obtained by skipping 20 print layers and thus had a nominal height h of 0.6 mm. The number of layers to be skipped was identified as the minimum number of layers to obtain a fully formed defect, without bridging of the flanks. Table 2 summarizes the type of test, notch type, build job, defect type and size and the numerosity of each test of the experimental campaign. The nomenclature employed for the benchmark specimens was the following:

- Specimen and loading type — T (Tensile), B (Bending) or B3D (Bending with 3D defects)

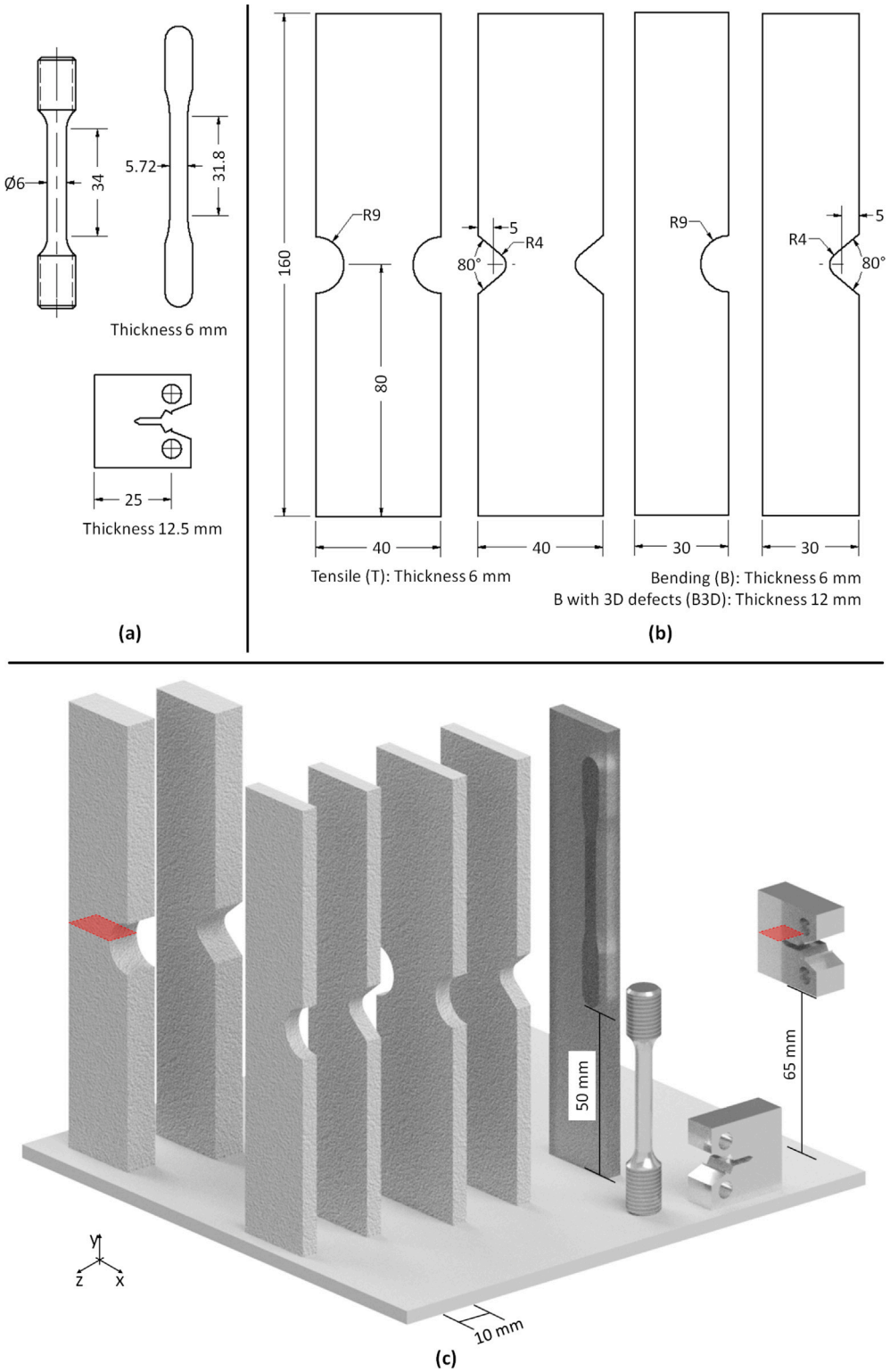

Fig. 1. Relevant geometrical dimensions in mm for (a) material characterization specimens and (b) benchmark specimens and (c) overview of the building layout.

Table 2
Experimental planning for the benchmark specimens.

Specimen	Notch	Defect type and size (Build job)	Numerosity	Total
Notched Tensile (T)	U (N1)	EDM through 1 mm (J1 $D1_E$)	1	
		2 mm (J1 $D2_E$)	2	
		0.25 mm (J1 $D0.25_E$)	2	
		Printed through 1 mm (J2 $D1_P$)	2	
		2 mm (J2 $D2_P$)	2	
		0.5 mm (J3 $D0.5_P$)	2	11
	V (N2)	EDM through 1 mm (J1 $D1_E$)	2	
		2 mm (J1 $D2_E$)	2	
		Printed through 1 mm (J2 $D1_P$)	2	
		2 mm (J2 $D2_P$)	2	8
Notched Bending (B)	U (N1)	EDM through 1 mm (J1 $D1_E$)	1	
		2 mm (J1 $D2_E$)	2	
		Printed through 1 mm (J2 $D1_P$)	2	
		2 mm (J2 $D2_P$)	2	8
	V (N2)	EDM through 1 mm (J1 $D1_E$)	2	
		2 mm (J1 $D2_E$)	2	
		Printed through 1 mm (J2 $D1_P$)	2	
		2 mm (J2 $D2_P$)	2	8
Notched Bending with 3D defects (B3D)	U (N1)	EDM semicircular R2 mm (J4 DS_E)	1	
		EDM rectangular 1 × 8 mm (J4 DR_E)	1	
		Printed semicircular R2 mm (J4 DS_P)	1	
		Printed rectangular 1 × 8 mm (J4 DR_P)	1	4
	V (N2)	EDM semicircular R2 mm (J4 DS_E)	1	
		EDM rectangular 1 × 8 mm (J4 DR_E)	1	
		Printed semicircular R2 mm (J4 DS_P)	1	
		Printed rectangular 1 × 8 mm (J4 DR_P)	1	4

- Notch type — N1 (U notch) or N2 (V notch)
- Build Job — J1, J2, J3 or J4
- Through thickness defect depth — D0.25, D0.5, D1 and D2 for 0.25, 0.5, 1 and 2 mm defects (subscript E for EDM defects; subscript P for printed defects)
- 3D defect type — DS for semicircular defects with radius of 2 mm and DR for 1 × 8 mm rectangular defects (subscript E for EDM defects; subscript P for printed defects)
- Progressive number — 1 or 2

Before testing, all the benchmark specimens with EDM defects were subjected to fatigue cycling under compression–compression loading conditions (compression pre-cracking) [41]. After compression pre-cracking, T and B specimens were analysed with a Zeiss light optical microscope to measure crack lengths on the sides. To obtain a clear image of the crack, the lateral surfaces were polished with sandpaper up to a grit of P800.

2.2.2. Testing

The tests on benchmark specimens were carried out in displacement control on an MTS Alliance RT 100 load frame, equipped with a 100 kN load cell. Two loading configurations were employed: for T benchmark specimens tensile loading was applied by clamping the specimens for 30 mm on both ends and imposing a crosshead displacement rate of 0.1 mm/min, while for B and B3D benchmark specimens three-point bending (3PB) loading was applied with a span of 110 mm and imposing a crosshead displacement rate of 0.2 mm/min. The maximum load reached during each test was recorded by the machine. For B and B3D benchmark specimens, experimental failure bending moments were computed as the recorded failure load divided by two and multiplied by the half-span (55 mm) of the 3PB setup. After the tests, the fracture surfaces were analysed with the same setup employed for the CT specimens described in Section 2.1. The measured crack length (a) for T and B specimens and crack depth and width (a, c) for B3D specimens is reported alongside specimen thickness B, remote width W_{rem} and width at the notch root W in Appendix B in Tables B.1, B.2 and B.3, respectively.

2.3. Microstructural and hardness analysis

Microstructural and hardness analyses of one benchmark specimen per build job were carried out to investigate the differences between Base and High material conditions. Portions of the four specimens were polished with sandpaper grit up to P2500. Vickers hardness (HV) was obtained following ASTM E92 [42] on ten points across the height, with a 300 g mass and 15 s of sinking time. After the hardness tests, the specimens were etched with Keller's reagent and the microstructure was observed with a Zeiss Sigma 500 Scanning Electron Microscope (SEM).

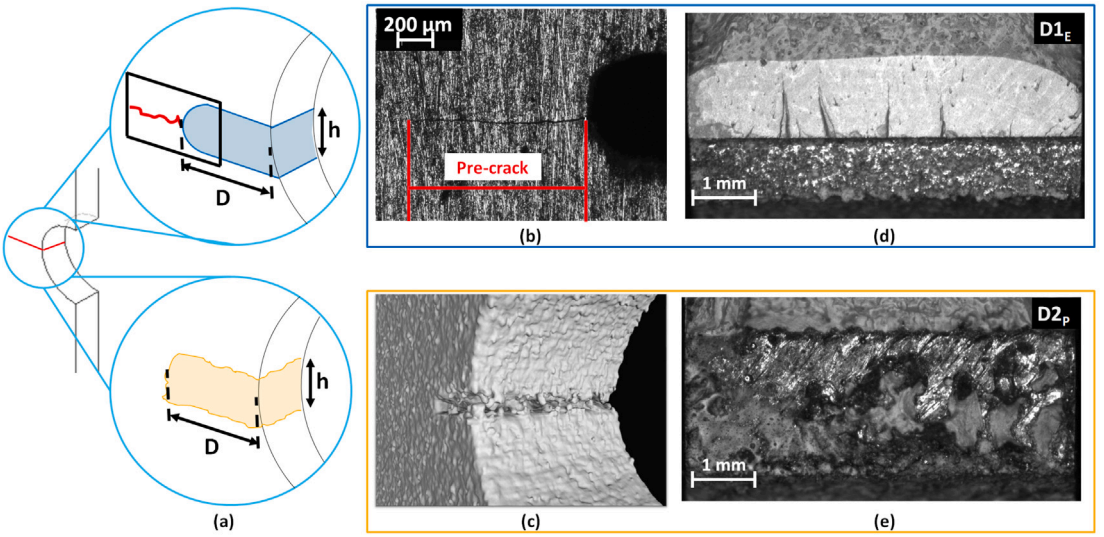

Fig. 2. Through defects on T and B benchmark specimens: (a) scheme highlighting the relevant defect dimensions; (b) side view of the pre-crack originating from an EDM defect; (c) printed defect observed with CT-scan; fracture surfaces of the specimens after testing for (d) an EDM defect and (e) a printed defect. For the EDM defect, it is possible to see the fatigue pre-cracking (b) on the specimen flank before the test and (d) on the fracture surface after the test.

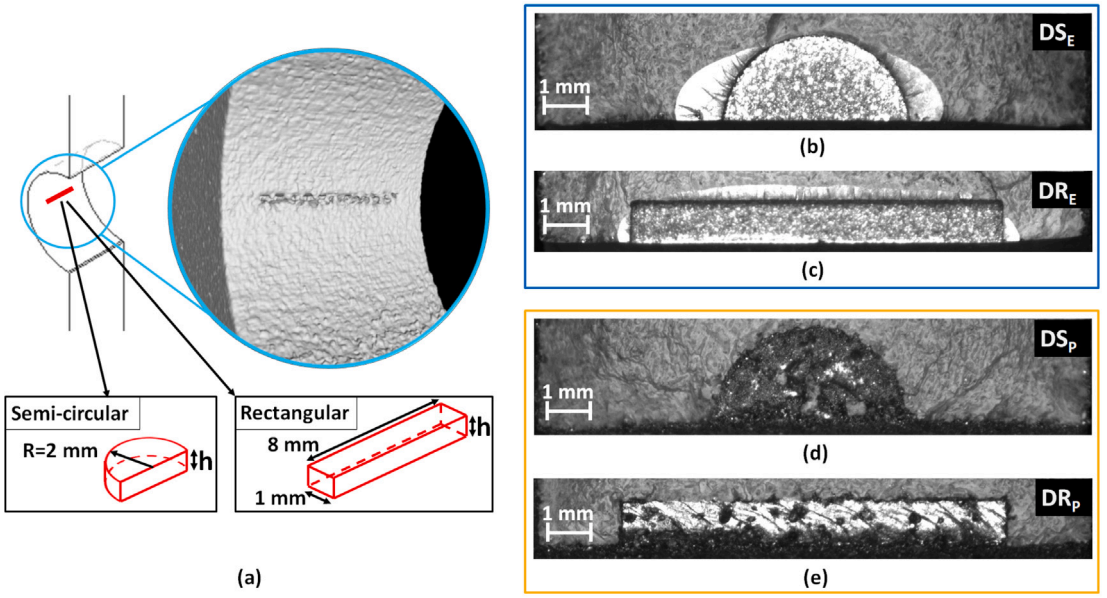

Fig. 3. Three-dimensional defects on B3D benchmark specimens: (a) example of printed defect and scheme of semicircular and rectangular 3D defects; fracture surfaces of the specimens after testing for (b) a semicircular EDM defect, (c) a rectangular EDM defect, (d) a semicircular printed defect and (e) a rectangular printed defect. For the EDM defects, it is possible to see the fatigue pre-cracking on the fracture surfaces.

Moreover, one Base and one High CT specimens were cut perpendicularly to the crack plane and then mirror-polished to obtain Inverse Pole Figure (IPF) maps using the SEM, equipped with Oxford Instruments' Electron Back-Scattered Diffraction (EBSD) detector model C-Nano. The mirror-polishing was carried out with a first phase of polishing with sandpaper grit up to P2500, followed by polishing with diamond suspension with particle size 1 μm and finally by vibro-polishing with colloidal silica.

Table 3
Monotonic and fracture toughness properties of this AlSi10Mg alloy as mean values and standard deviations.

Position	Build job	Monotonic properties				Fracture toughness	
		$R_{p,0.2\%}$ [MPa]	R_m [MPa]	ε_f [%]	n [–]	$J_{I,c}$ [N/mm]	$K_{I,c}$ [MPa$\sqrt{\text{m}}$]
Base	J1	240 ± 1	398 ± 2	3.94 ± 0.05	0.201	7.3 ± 0.3	23.8 ± 0.6
	J2	246 ± 2	413 ± 4	4.44 ± 0.14	0.199	6.6 ± 0.0	22.6 ± 0.1
	J3	218 ± 3	375 ± 1	4.03 ± 0.09	0.218	6.7 ± 0.7	22.7 ± 0.6
	J4	225 ± 4	384 ± 4	4.04 ± 0.10	0.227	6.7 ± 0.2	22.9 ± 0.6
High	J2	207 ± 2	362 ± 4	3.93 ± 0.21	0.212	10.6 ± 0.5	28.7 ± 1.2
	J3	–	–	–	–	12.1 ± 1.1	30.7 ± 1.4
	J4	–	–	–	–	12.6 ± 1.0	31.6 ± 1.5

3. Results

3.1. Material characterization

3.1.1. Monotonic properties

The tensile curves obtained from tests on tensile specimens are shown in Fig. 4(a), while the resulting monotonic properties are reported in Table 3: namely, the yield strength corresponding to 0.2% plastic strain $R_{p,0.2\%}$, the ultimate tensile stress R_m, the strain at failure ε_f and strain hardening exponent n. The strain hardening exponent n was obtained by a least-squares fitting of the Ramberg–Osgood equation [43]:

$$\varepsilon = \frac{\sigma}{E} + 0.002\left(\frac{\sigma}{R_{p,0.2\%}}\right)^{1/n} \tag{1}$$

3.1.2. Fracture toughness

As for fracture toughness tests, Fig. 4(b) shows the R-curves obtained from the fracture toughness tests. The resulting $J_{I,c}$ values were computed according to ASTM E1820 [40] and the equivalent $K_{I,c}$ was calculated as:

$$K_{I,c} = \sqrt{\frac{E}{(1-\nu^2)}J_{I,c}} \tag{2}$$

where elastic modulus E and Poisson's ratio ν were assumed equal to 70 000 MPa and 0.3, respectively. The obtained fracture toughness parameters are reported in Table 3.

The fracture surfaces of representative tensile and CT specimens for Base and High locations were investigated with SEM at 500x and 7000x magnifications and are reported, respectively, in Figs. A.2 and A.3 in Appendix A.

The monotonic [10,11,44–55] and fracture toughness [10,11,51–55] properties obtained from Base specimens were comparable with data from literature on the same AlSi10Mg alloy produced by L-PBF in the AB condition with loading direction parallel to the building direction (y axis). However, it is interesting to see how High specimens showed a more pronounced R-curve behaviour than Base specimens, with a significantly increased resistance to crack growth, despite the ductility of tensile specimens being slightly lower than for Base specimens. This could be attributed to the different thermal history at different heights from the base plate producing different microstructure and thus inducing significantly different material properties.

Fig. 5 shows a comparison of R_m, ε_f and $J_{I,c}$ values between the present study and the literature on AlSi10Mg alloy produced by L-PBF for specimens with loading direction parallel to the building direction (y axis) considering three different material conditions:

- AB [11,51–54];
- direct ageing (DA) at 200 °C for 4 h [54,55];
- stress relieving (SR) at 300 °C for 2 h [53,55].

The data shows significant correlation between $J_{I,c}$ and ε_f and between $J_{I,c}$ and R_m. Moreover, it is interesting to see how the AB and DA fracture properties are very close, thus confirming that AB manufacturing route can be adopted for parts subjected to static loads.

3.1.3. Microstructural and hardness analysis

EBSD analyses were carried out on one Base CT specimen and one High CT specimen to investigate the difference in the observed fracture toughness properties. The resulting IPF X maps and grain size diameter distributions are reported in Fig. 6 and show no evident difference between the two investigated conditions.

Therefore, the microstructure of this AlSi10Mg alloy was further investigated and the results are shown in Fig. 7(a), highlighting the differences between inner melt pool and melt pool tracks as well as the differences observed at different heights from the base plate, namely High (y ≈ 140 mm) and Base (y ≈ 20 mm) locations. Pictures at high magnification showed a solidification structure characterized by cellular-dendritic patterns. The darker cellular features, identified as primary Al, were intricately decorated with white Si networks. Additionally, the coarse cellular zone at the melt pool boundary, where the cooling rate is lower due to the

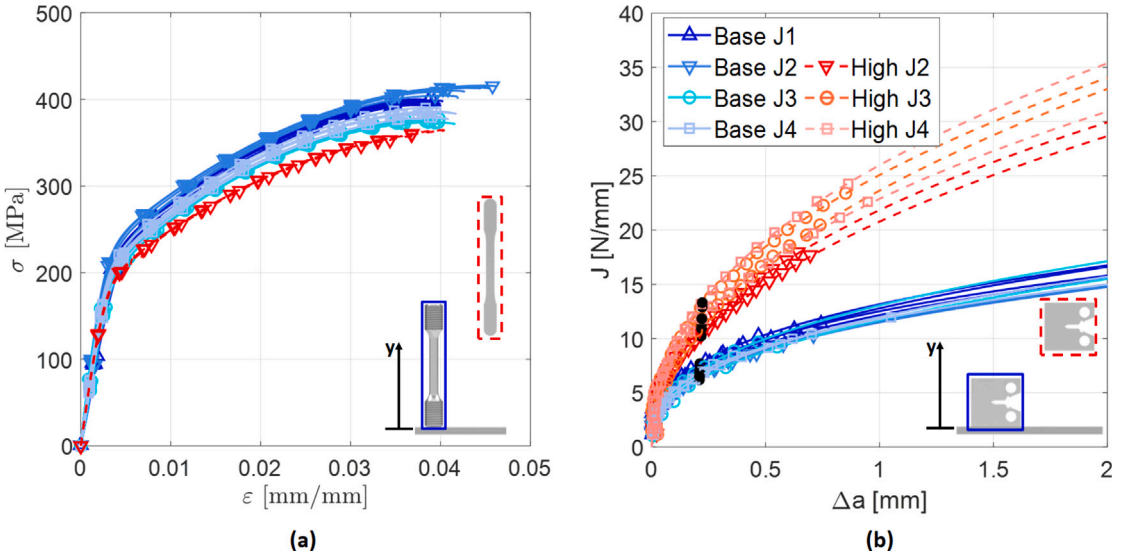

Fig. 4. Material properties: (a) monotonic tensile curves; (b) J-R curves for this AlSi10Mg alloy. Blue curves represent Base specimens, while red curves represent High specimens.

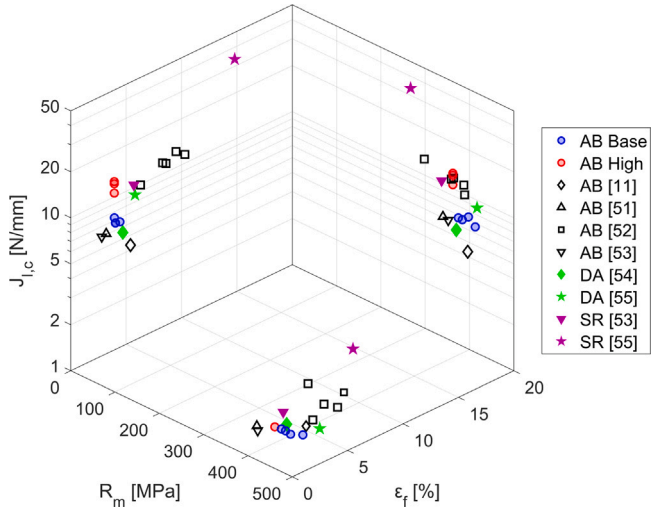

Fig. 5. Comparison of monotonic and fracture toughness material properties for this AlSi10Mg alloy and literature data on AlSi10Mg alloy produced by L-PBF in the AB, DA and SR conditions.

Gaussian distribution of laser energy, contributed to the observed enlargement of cellular structures. This observation aligns with findings reported by other studies involving AlSi10Mg samples produced by L-PBF [56,57]. The Si network exhibited elongation along the build direction (y axis), as depicted in the high magnification pictures in Fig. 7(a). The morphology of the Base locations displayed a distinctive microstructure characterized by an interconnected Si network accompanied by additional intracellular precipitation of Si particles. This variation is linked to an extended exposition to high temperatures during the holding period, fostering increased diffusion. Consequently, the Si network underwent a transformation into a spheroidized structure, with Si precipitates within the Al cells [58,59]. Furthermore, a notable trend in HV can be observed in Fig. 7(b), with higher values in the Base location gradually diminishing towards the High location. This variation aligns with insights from existing literature, specifically emphasizing that the mechanical properties observed in L-PBF samples are not solely a result of a very fine microstructure, but they are also influenced by precipitation hardening, a phenomenon induced by the self-quenching effect during the manufacturing process [60]. Additionally, the Si precipitation, particularly evident in Base specimens, could contribute significantly to the higher HV values observed.

The higher precipitation density in the Base condition, with Si precipitates acting as stress raisers, may promote crack propagation. Observations of fracture surfaces from tensile specimens support this hypothesis (Fig. A.2 in Appendix A). In fact,

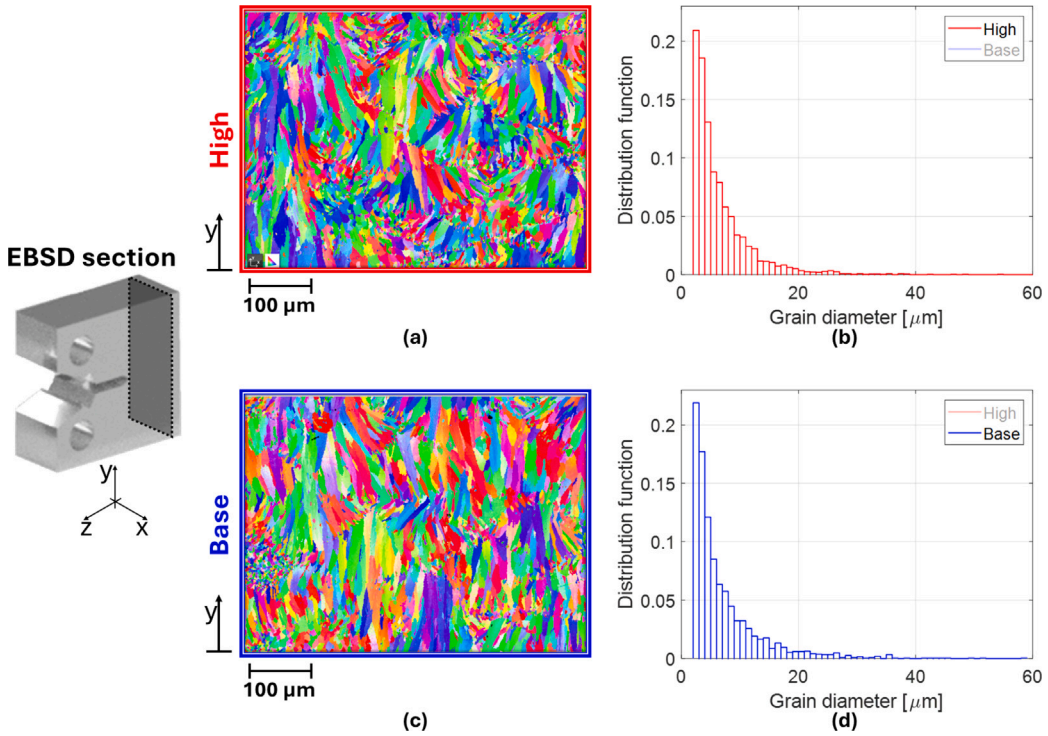

Fig. 6. IPF X maps of (a) High and (c) Base CT specimens from EBSD, observed perpendicular to the building direction y, and related grain size diameter distribution for: (b) High and (d) Base locations.

fracture surfaces of Base tensile specimens appeared smoother, suggesting brittle fracture, while those from the High condition displayed more pronounced dimples, characteristic of ductile fracture. Moreover, the High specimens showed a less connected Si network and lower precipitation density (Fig. 7(a)), leading to improved Al matrix ductility and significantly higher fracture toughness. Finally, the SEM analysis of the fracture surface of the High CT specimen reveals the presence of secondary cracks (Fig. A.3(b) in Appendix A). Secondary cracks tend to form when the crack changes its path, i.e. when the crack follows a tortuous crack path. The High specimens showed a more tortuous crack path, as can be seen in Fig. A.3, in which the fracture surface in the test region appears rougher than for the Base specimens. These secondary cracks play a crucial role in dissipating energy and delaying primary crack growth, contributing to the overall enhanced fracture toughness observed for the High fracture toughness properties [54].

Therefore, considering that the test regions of the High material characterization specimens have the same distance from the building platform as the crack plane of the benchmark specimens, the material properties employed for static fracture assessment were the ones obtained with the High specimens.

3.2. Fracture benchmark specimens

The failure loads versus crack size of T benchmark specimens are reported in Fig. 8(a), while Fig. 8(b) and (c) depict the failure bending moments versus crack size for the B and B3D benchmark specimens, respectively. Each point represents a benchmark specimen: empty markers represent specimens with EDM defects, while filled markers represent printed defects. For T and B benchmark specimens, circles represent U notch specimens, while triangles represent V notch specimens. For B3D benchmark specimens, each type of marker represents a different combination of defect and notch: circles represent U notch with semicircular defects, squares represent U notch with rectangular defects, upward facing triangles represent V notch with semicircular defects and downward facing triangles represent V notch with rectangular defects.

It is possible to appreciate how there are no significant differences between EDM defects with fatigue cracks and printed defects. This is likely due to the quasi-brittle material behaviour of this AlSi10Mg alloy. It can also be noted how the failure loads decrease with the crack length, as may be expected by the related increase in CDF. It is important to notice that the stress concentration factor K_t, defined as the ratio between the maximum stress perpendicular to the crack plane at the root of the notch and the maximum remote stress, was 3.17 for U notch and 4.29 for V notch T benchmark specimens and 3.14 for U notch and 4.14 for V notch B benchmark specimens. Therefore, the lower failure loads observed for V notch specimens with crack lengths comparable to U notch specimens are likely due to the higher local stress on the crack plane for the same remote load. All experimental failure loads for T (F_{EXP}), B and B3D (M_{EXP}) benchmark specimens are reported in Appendix C in Tables C.1, C.2 and C.3, respectively.

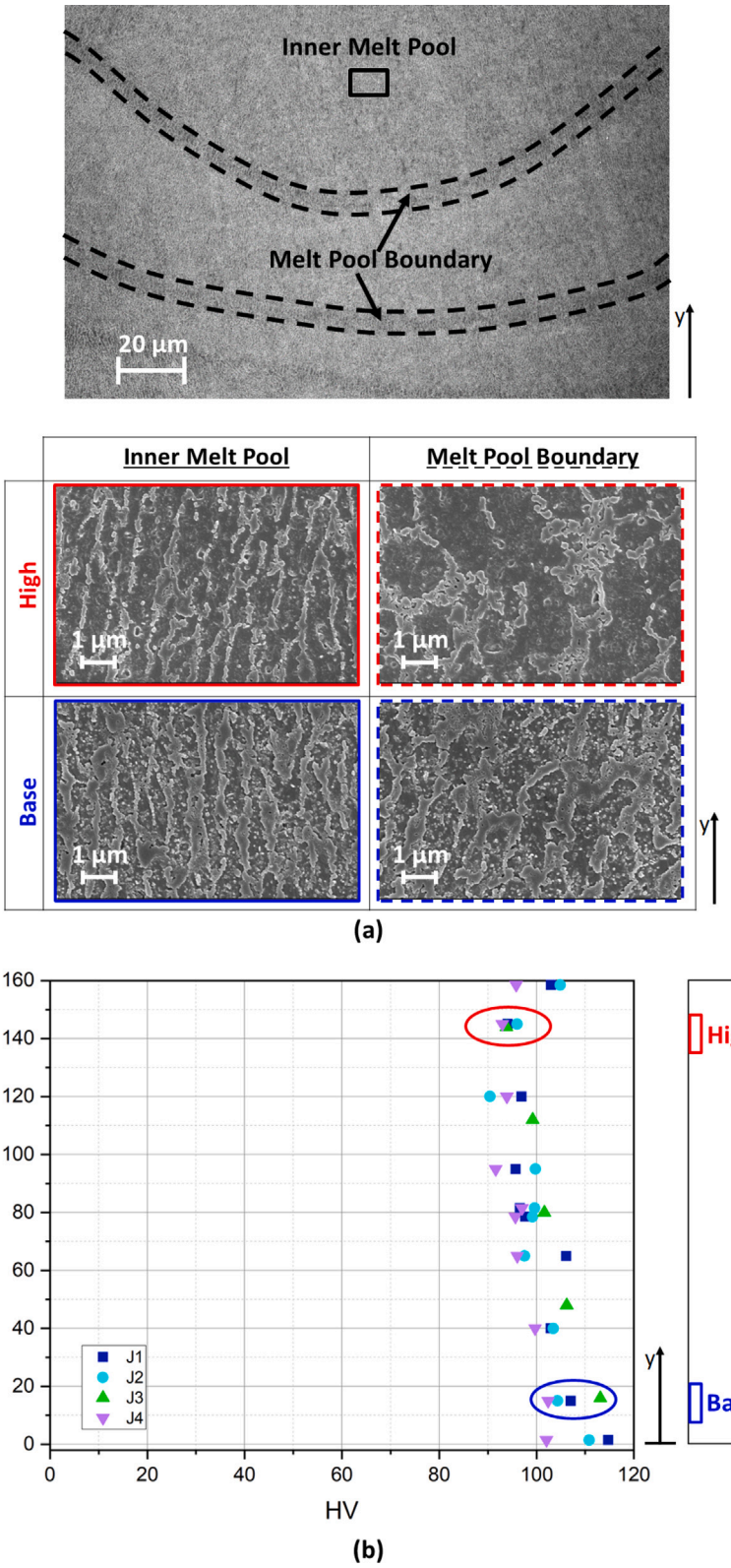

Fig. 7. Microstructure and micro-hardness analyses: (a) zones of the melt pool and microstructure of the inner melt pool and of the melt pool boundaries for high and base locations; (b) Vickers hardness measured at different printing heights on benchmark specimens.

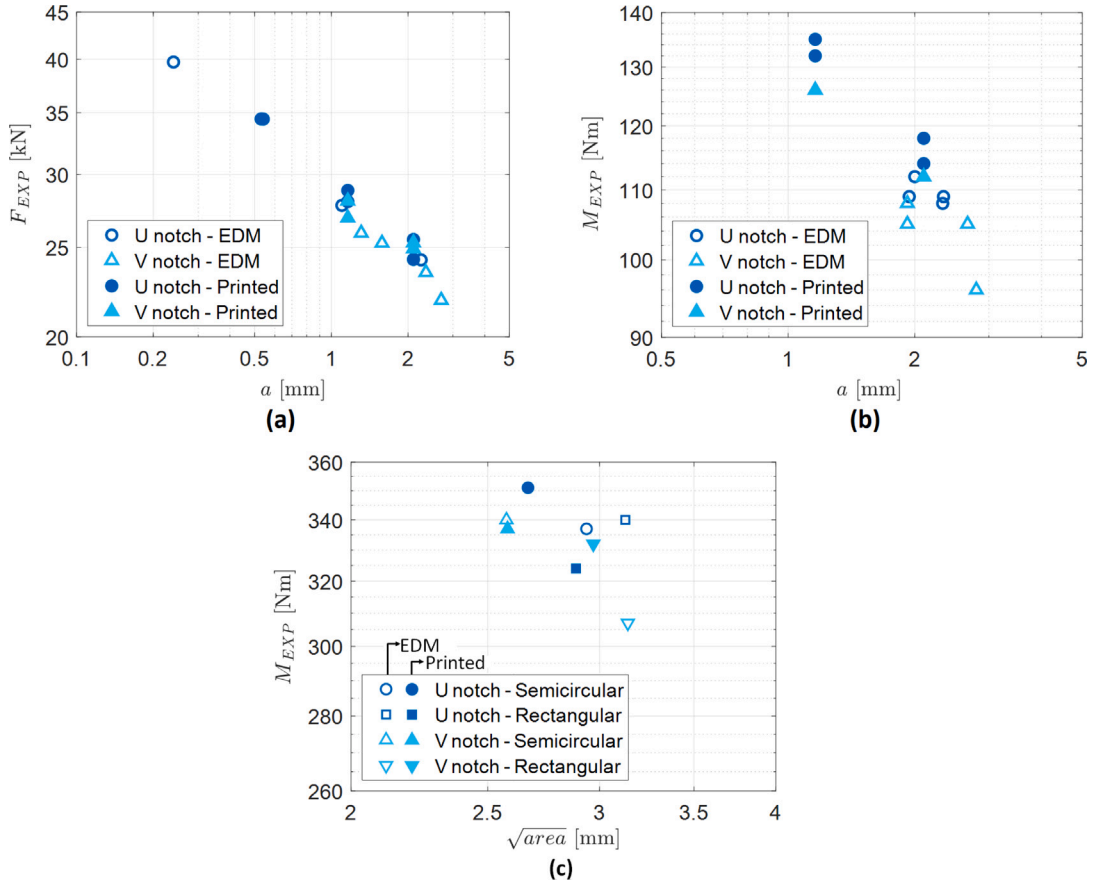

Fig. 8. Failure load versus crack size for: (a) T benchmark specimens, (b) B benchmark specimens and (c) B3D benchmark specimen. For B3D benchmark specimens the crack size is expressed as $\sqrt{area}$.

4. Computational crack driving force analyses of fracture experiments

The static fracture of all benchmark specimens was investigated using the computational CDF approach. Following the conclusions drawn from previous works on static fracture of AB AlSi10Mg manufactured by L-PBF [11], the EPFM parameter J-integral was selected as the relevant descriptor of CDF, since it allows to take into account the significant effect of small-scale plasticity on this AlSi10Mg alloy. The J-integral was computed with dedicated FE analyses using Simulia Abaqus by Dassault Systèmes, employing Von Mises yield surface [43]. The authors decided to predict failure by comparing the CDF with the fracture toughness $J_{I,c}$, rather than by performing an assessment employing the material R-curve for the sake of simplicity of the analyses. In fact, the increased accuracy attainable with the R-curve approach comes at the price of several FE models for each investigated specimen. Therefore, the effort required was deemed excessive, given that the CDF approach using $J_{I,c}$ already proved to be capable of predicting failure loads with good accuracy for this AlSi10Mg alloy [11]. The calibration of the material model considered the approximation of the true stress–strain curves by means of the Ramberg–Osgood equation (Eq. (1)), while the elastic modulus and the Poisson's ratio were set to $E = 70\,000$ MPa and $\nu = 0.3$, respectively.

4.1. Notched tensile specimens

2D FE models of the T benchmark specimens were developed using the crack plane xz (Fig. 9(a)) as the plane of symmetry. Cracks have been reproduced considering their average length, evaluated from the fractographies after specimens' failure (Appendix B). The symmetry condition was then applied on the crack plane. The simulations were carried out with 8-node quadratic quadrilateral plane stress elements with reduced integration (CPS8R). The dimension of the elements was set to approximately 100 μm in the region within 2 mm from the crack plane (Fig. 9(b)). The mesh size was defined after evaluating convergence of J-integral with a more refined mesh of 50 μm. The FE simulations were performed by applying a remote incremental displacement to a reference point which was kinematically coupled with the top surface (Fig. 9(a)), which emulated the bending restraint of the experimental set-up. As output, the axial reaction force was considered together with the J-integral values for different contours along the crack front. Convergence of J-integral values was obtained for contour numbers higher than 6.

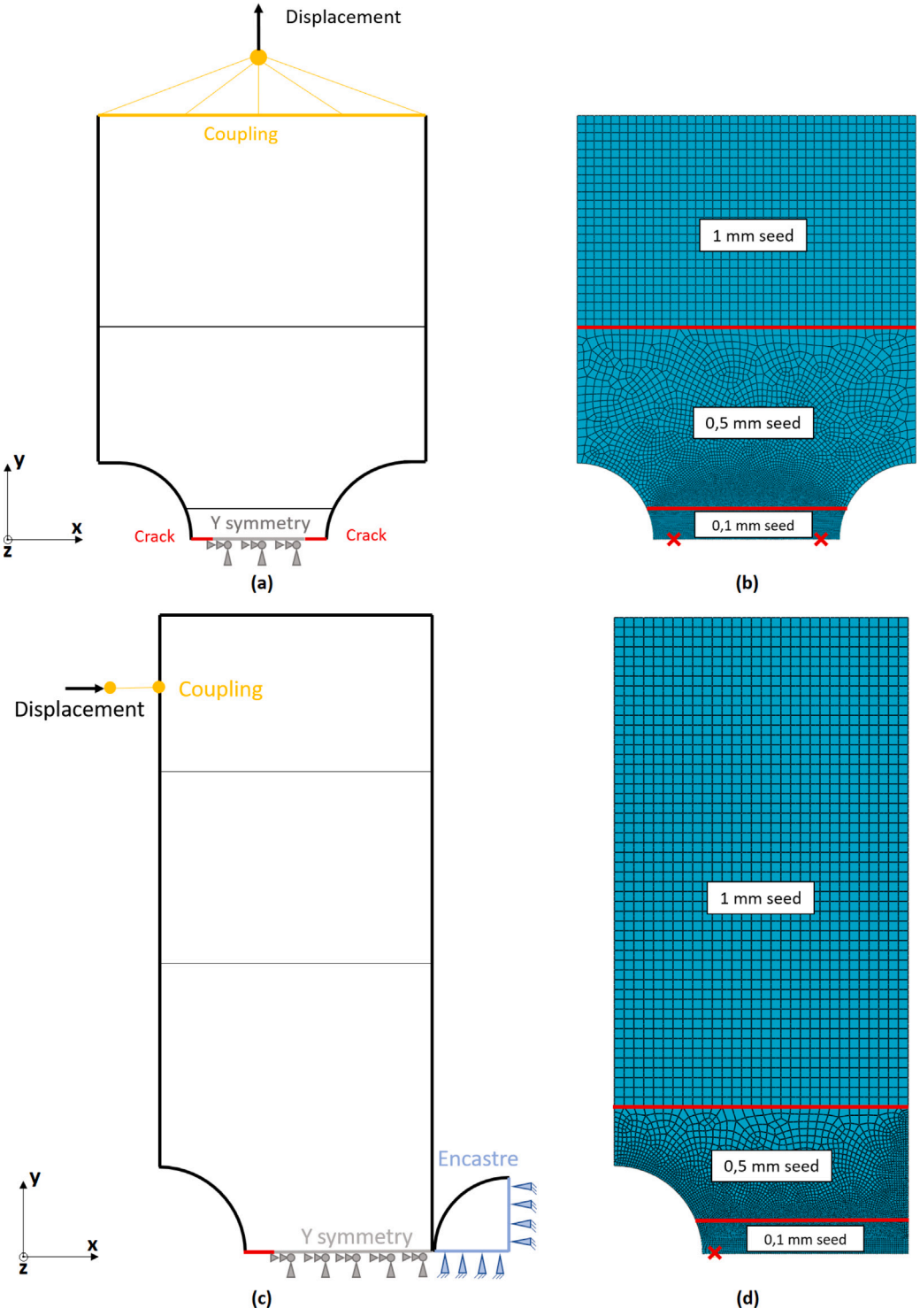

Fig. 9. FE analysis of T and B benchmark specimens: (a,c) FE setup and (b,d) seed strategy.

4.2. Notched bending specimens

Analogously to T benchmark specimens, the FE simulations of the B benchmark specimens test setup was accomplished by means of a 2D model, exploiting the symmetry along the crack plane xz. To simulate the 3PB configuration, the top roller was recreated with a 1/4 model with all 3 degrees of freedom constrained and a remote incremental displacement was applied to a reference point kinematically coupled with the nodes in correspondence of the bottom roller (Fig. 9(c)). A generic steel with elastic modulus E = 207 000 MPa and Poisson's ratio $\nu = 0.33$ was considered for the roller. As for the notched tensile specimens, the dimension of the elements was set to approximately 100 μm in the region within 2 mm from the crack plane (Fig. 9(d)). The outputs of the analyses were the reaction force at the reference point and the J-integral. Convergence of the J-integral was obtained for contour numbers higher than 6.

4.3. Notched bending specimens with 3D defects

The FE simulations of the B3D benchmark specimens were carried out by means of a 3D model, exploiting the symmetry along the crack plane xz as well as the symmetry of the 3D defects on the xy plane (Fig. 10(a)). The top roller of the 3PB configuration was simulated by fully constraining (encastre) a region of 3 mm from the crack plane xz. The load was imposed via a remote incremental displacement applied to a reference point kinematically coupled with the nodes in a 2 mm region corresponding to the bottom roller (Fig. 10(a)). The dimension of the elements was set to approximately 100 μm in the region within 2 mm from the crack plane (Fig. 10(b)). The outputs of the analyses were the reaction force at the reference point and the J-integral. Convergence of the J-integral was obtained for contour numbers higher than 6.

4.4. Results and discussion

In Fig. 11(a) the CDF of a T benchmark specimen is represented with a solid blue line as the square root of the J-integral $\sqrt{J}$, to better evidence the contribution of plasticity which is moving the curve away from the linear elastic behaviour, shown with a dashed blue line as $\sqrt{J_{el}}$. The linear elastic J-integral $\sqrt{J_{el}}$ was obtained by a linear extrapolation of the first two points of the $\sqrt{J}$, considering no contribution of plasticity for the low load values at which the J-integral was computed. The average fracture toughness of the High CT specimens, in terms of $\sqrt{J_{I,c}}$, is represented as a horizontal solid black line, while the dashed black lines represent the one standard deviation scatter band. The experimental failure load is depicted as a vertical dashed red line. The failure load estimated from the FE model was obtained as the intersection between the fracture toughness $\sqrt{J_{I,c}}$ and the increasing $\sqrt{J}$ and is represented by a blue dot. A comparison between experimental failure loads and predictions from computational CDF analyses is shown in Fig. 11(b) for T benchmark specimens, Fig. 11(c) for B benchmark specimens and Fig. 11(d) for B3D benchmark specimens. The dashed black line represents the complete agreement between predicted and experimental failure loads (0% error), while the dashed grey lines represent the ±10% error band. For all benchmark specimens, the CDF predictions were conservative, and most points were between the 0% and the −10% error band. These results confirm that the failure of AlSi10Mg components manufactured by L-PBF is well described by EPFM when considering mechanical properties consistent with the crack location. All CDF results for T ($F_{FAD,numerical}$), B ($M_{FAD,numerical}$) and B3D (M_{CDF}) benchmark specimens are respectively reported in Tables C.1, C.2 and C.3 in Appendix C. Results for T and B benchmark specimens are reported as FAD numerical due to the overlap between the two approaches, as it will be explained in the next Section 5.

5. Failure assessment diagram analyses

In Section 4, we showed how a numerical approach that accounts for specimen geometry, crack size and relevant material properties is capable of predicting with high accuracy the failure loads of benchmark specimens. Nevertheless, carrying out numerical simulations with elastic–plastic material properties is often complex and time-consuming. It was already proven that FAD analyses were capable of good predictions for failure loads of thin plain geometries under tensile and bending loading conditions [11]. In this Section we investigate the adoption of the FAD on the thin notched benchmark specimens.

The FAD approach allows to approximate the elastic–plastic crack driving force J for a given load P as [19]:

$$J(P) = K^2(P)/E' \cdot f(L_r)^{-2} \tag{3}$$

where K is the SIF and L_r is the ligament yielding, defined as the ratio between P and the plastic collapse load of the cracked section P_0, while E' is equal to E for plane stress conditions and to $E/(1-\nu^2)$ for plane strain conditions. The function $f(L_r)$ is monotonically decreasing for increasing values of L_r up to $L_{r,max} = \sigma_{flow}/R_{p,0.2\%}$, which accounts for hardening and thus for materials failing at flow stress ($\sigma_{flow} = (R_m + R_{p,0.2\%})/2$) rather than at yield strength. In particular, $f(L_r) < 1$ for $P > 0.3 \cdot P_0$ to take into account the increased driving force due to plastic strains ahead of the crack tip [33]. FAD analysis is carried out with the following steps:

1. Selection of a substitute geometry, considering part geometry and crack shape.
2. Calculation of K and P_0 for the substitute geometry and the given load P.
3. Calculation of non-dimensional parameters $\bar{K}_r = K/K_{I,c}$ and $\bar{L}_r = P/P_0$.

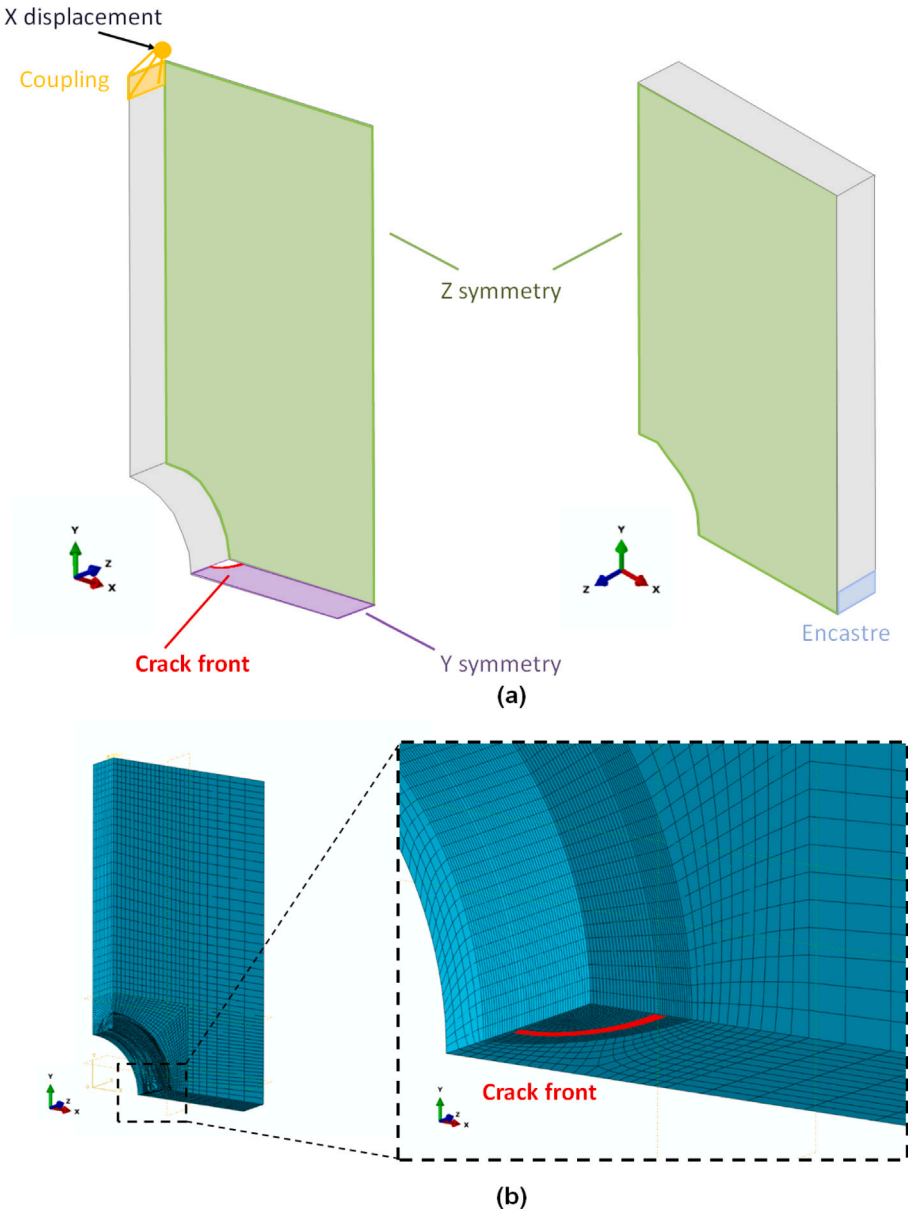

Fig. 10. FE analysis of B3D benchmark specimen: (a) FE general model; (b) detail of the modelled crack front.

4. Assessment of component design as safe if the assessment point $(\bar{L}_r, \bar{K}_r)$ lies below the limit curve $K_r = f(L_r)$ in the $L_r K_r$ plane, or potentially unsafe otherwise.

The FAD procedure is actively employed in the oil and gas and nuclear sectors and is defined by standards as an "Option-based assessment" [15,20,21]. Each "Option" is given a progressive number corresponding to an increase with the complexity of the analysis and the required material information. Using BS7910 nomenclature, three Options are defined as follows:

1. Option 1 requires knowledge of the yield strength, ultimate tensile stress and fracture toughness for the material.
2. Option 2 requires knowledge of the complete true stress–strain curve and fracture toughness.
3. Option 3 requires carrying out FE simulation to obtain linear elastic and elastic–plastic crack driving force and knowledge of the fracture toughness.

Each Option employs a different definition of the limit curve $f(L_r)$. The different $f(L_r)$ curves are formulated as semi-empirical relationships between material properties and elastic–plastic CDF. For an exhaustive and thorough description of the FAD procedure, the reader is referred to Zerbst's book [19]. In this work, Option 2 was selected for the analyses, for which the limit curve is defined

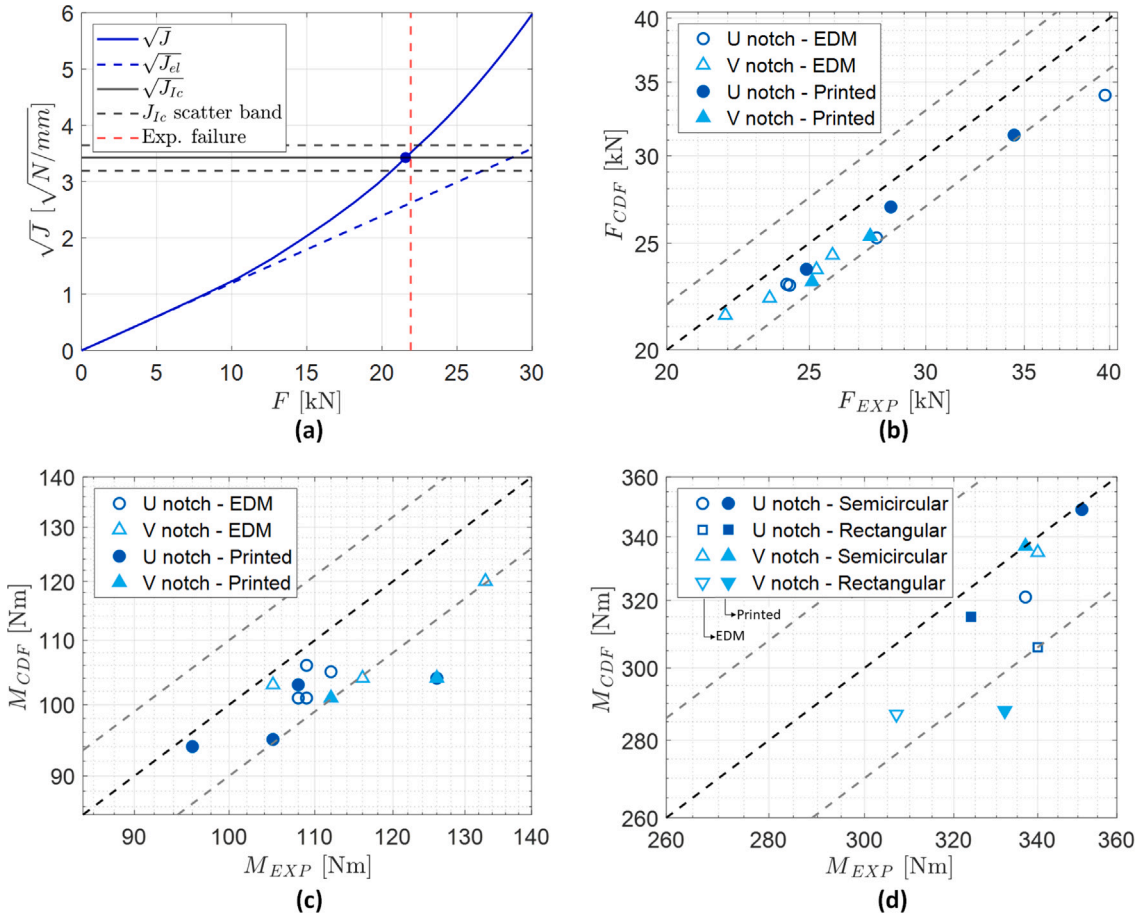

Fig. 11. Crack Driving Force analyses for T, B and B3D benchmark specimens: (a) example of CDF diagram for a T benchmark specimen; comparison of predicted failure loads with the numerical CDF approach versus experimental failure loads for (b) T benchmark specimens, (c) B benchmark specimens and (d) B3D benchmark specimens.

in BS7910 as:

$$f(L_r) = 1/\sqrt{\frac{E \cdot \varepsilon_{ref}}{\sigma_{ref}} + \frac{L_r^2 \cdot \sigma_{ref}}{2 \cdot E \cdot \varepsilon_{ref}}} \tag{4}$$

where the reference stress $\sigma_{ref} = L_r \cdot R_{p,0.2\%}$ and the reference strain ε_{ref} is the strain corresponding to σ_{ref} on the true stress–strain curve.

The substitute geometry for T and B benchmark specimens was a plate with an edge crack with thickness equal to 6 mm and width equal to the net section at the root of the notch. For T benchmark specimens each crack was investigated separately, thus only half width was considered. The SIF was computed from the CDF results of the FE analyses described in Section 4 as:

$$K(P) = \sqrt{J_{el}(P) \cdot E} \tag{5}$$

The plastic collapse load P_0 was computed with three methods:

- Using the component-based numerical approach proposed by Zerbst et al. [61,62].
- Using BS 7910 reference stress solutions for the substitute geometry.
- Using simplified analytical formulations on the net cracked sections.

5.1. Numerical formulation

Values of K and P_0 were obtained from the FE analyses described in Section 4 for a generic load P. The SIF can be obtained as $K = \sqrt{J_{el} \cdot E}$, where J_{el} is the elastic part of the J-integral evaluated numerically (Fig. 11(a)). With reference to BS7910, the Option

3 limit curve can be defined from numerical results as:

$$f(L_r) = \sqrt{\frac{J_{el}(P)}{J(P)}} \tag{6}$$

An example of Option 3 limit curve is depicted in blue in Fig. 12(a). The P_0 is computed as the load for which $f(L_r)$ for Option 3 is equal to $f(L_r = 1)$ for Option 2. Once we evaluated the numerical K and P_0 it is possible to define the K_r and L_r ratios for the generic load P, plot the limit curve and predict the failure condition. The same procedure was applied on all T and B benchmark specimens and the resulting predicted failures ($F_{FAD,computational}$ and $M_{FAD,computational}$) were compared with the experimental failures in Fig. 12(c,d), respectively, and are reported in Tables C.1 and C.2 in Appendix C. The results show that the FAD approach can accurately predict experimental failures when numerical K and P_0 solutions are employed, as expected by the accurate estimates obtained with the numerical CDF approach in Section 4.

5.2. BS7910 analytical formulations

The objective of FAD analyses is to provide simple solutions that do not require complex FE simulations. For this purpose, many analytical solutions for K and P_0 were developed and collected in compendiums. The reference standard we considered is BS7910 [15], which provides solutions for a wide range of simple geometries. These solutions require the identification of the most representative substitute geometry and to evaluate the tensile and bending stress components in the non-cracked specimens, either from numerical analyses or from experiments, with a generic load P imposed. In BS7910, most collapse load solutions are presented in the form of a reference stress σ_{ref}, for which $L_r = \sigma_{ref}/R_{p,0.2\%}$ and thus $P_0 = P \cdot R_{p,0.2\%}/\sigma_{ref}$. To be consistent with the previously discussed computational analyses, all the calculations were carried out considering the K from numerical analyses to better reveal the effect of the different P_0 estimates. This decision was made to disregard the dependence on the quality of the K solution, since the one from BS7910 was found to be highly conservative compared to the numerical one. The results with the P_0 solution from BS7910 are reported in Appendix C Table C.1, for T benchmark specimens ($F_{FAD,BS7910}$), and Table C.2, for B benchmark specimens ($M_{FAD,BS7910}$). Failure loads predicted using BS7910 show a high level of conservatism for all T and B benchmark specimens, with errors ranging between 25% and 45% with respect to the experimental loads.

5.3. Simplified analytical formulations

Simple analytical P_0 load solutions have been tested for both T and B benchmark specimens and they have been applied to identify the failure load through the FAD approach together with K from numerical analyses.

For T benchmark specimens, a method capable of accounting for the actual state of stress ahead of the crack was investigated. Hence, the stress distribution normal to the crack plane obtained through FE analysis on a non-cracked specimen $\sigma(x)$ has been normalized with respect to the applied remote stress $\sigma_{rem,FE}$. The normalized distribution $\sigma(x, \sigma_{rem})$ was, thus, a linear function of the remote stress σ_{rem} (Eq. (7)). The normalized stress state was then integrated, equated to the plastic collapse load of the ligament section and the equation was solved with respect to the remote stress. The tensile P_0 load (F_0) was finally obtained by multiplying the obtained remote stress σ^*_{rem} by the area of the remote section.

$$\begin{aligned} &\sigma(x, \sigma_{rem}) = \frac{\sigma(x)}{\sigma_{rem,FE}} \cdot \sigma_{rem} \\ &\int_a^W \sigma(x, \sigma_{rem}) dx = R_{p,0.2\%} \cdot (W - a) \\ &F_0 = \sigma^*_{rem} \cdot W_{rem} \cdot B \end{aligned} \tag{7}$$

The analytical method proposed for the evaluation of P_0 for B benchmark specimens (M_0) was to estimate the bending moment for which the specimen's ligament section is in plastic collapse conditions, neglecting the stress concentration of the notch. This load corresponds, for rectangular sections, to 1.5 times the load that causes first yielding $M^*_{I,p}$, corrected to account for the partialization of the section due to the crack (Eq. (8)).

$$M_0 = 1.5 \cdot M^*_{I,p} \cdot \left(1 - \frac{a}{W}\right)^2 = 1.5 \cdot \frac{R_{p,0.2\%} \cdot W^2 \cdot B}{6} \cdot \left(1 - \frac{a}{W}\right)^2 \tag{8}$$

Tables C.1 and C.2 in Appendix C report the failure load predictions obtained through FAD approach for T ($F_{FAD,simplified}$) and B ($M_{FAD,simplified}$) benchmark specimens using the simplified analytical formulations. The predicted failure loads are close to the experimental failure loads, albeit slightly conservative, with a maximum error of $\approx 15\%$.

It is important to underline that the significant scatter of reference load P_0 shown by the formulations employed in this study (Fig. 12(c,d)) is related to the fact that the investigated FAD approaches have very different practical applications. The component-based numerical approach proposed by Zerbst et al. [61,62] provides accurate results but should be employed to compute parametric formulations of the failure line $f(L_r)$ for a given combination of component and crack geometries rather than for individual cases. The reference stress solution of BS7910 provides conservative estimates for the investigated cases, likely caused by the presence of the stress concentration on the crack plane. On the other hand, the simplified analytical formulations stem from the concept of plastic collapse of the ligament, which better accounts for the stress distribution ahead of the notch.

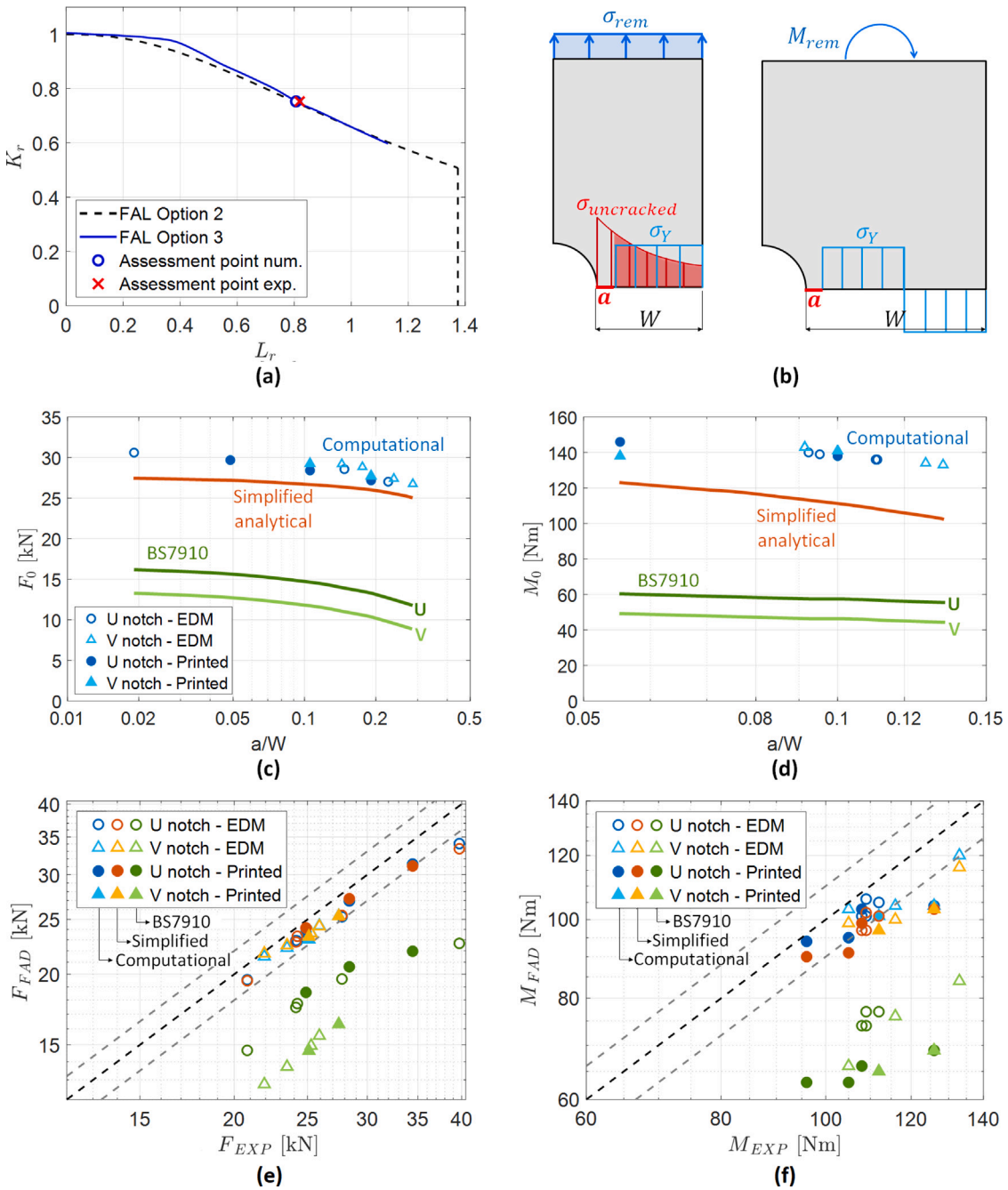

Fig. 12. Failure Assessment Diagram analyses for T and B benchmark specimens without residual stresses: (a) example of FAD for a T benchmark specimen; (b) models for the computation of F_0 and M_0 with the simplified analytical approach; comparison of collapse loads versus a/W ratio for FE and analytical formulations of (c) F_0 for T benchmark specimens and (d) M_0 for B benchmark specimens; comparison of predicted failure loads using the FAD versus experimental failure loads for (e) T benchmark specimens and (f) B benchmark specimens.

5.4. Effect of residual stresses

The potential impact of residual stresses on the predicted failure was investigated with the framework reported in BS7910, in which the increased CDF due to residual stresses is considered as:

$$K_r = \frac{K_I + V \cdot K_{rs}}{K_{I,c}} \tag{9}$$

where K_{rs} is the SIF due to residual stresses and the value of V is computed with the following equation:

$$V = \begin{cases} \min\left(1 + 0.2 \cdot L_r + 0.02\dfrac{K_{rs} \cdot L_r}{K_I} \cdot (1 + 2 \cdot L_r); 3.1 - 2 \cdot L_r\right) & \text{for } L_r < 1.05 \\ 0.4 & \text{for } L_r \geq 1.05 \end{cases} \tag{10}$$

The residual stress profile ahead of the notch was assumed the same as the one in the printing direction for DA net shape specimens reported in [63,64], while the measured residual stress on the surface was similar to AB net shape specimens [65,66]. The K_{rs} was then estimated with NASGRO v10.11, employing the geometry for through cracks at the edge of a notch in a finite plate (TC17) for T and B benchmark specimens. The NASGRO software was employed to exploit the higher precision of the weight function formulations compared to the simplified analytical formulations of BS7910. The resulting values of K_{rs} ranged from 2 to 5.5 MPa$\sqrt{\text{m}}$.

The failure loads estimated with the three FAD formulations for plastic collapse are reported in Tables C.4 and C.5 in Appendix C, for T and B benchmark specimens, respectively. Failure loads estimated without residual stresses were also reported in the same tables, to allow a direct comparison. Failure loads with residual stresses computed with BS7910 formulations were the same as the one computed without residual stresses, since the predicted failure always occurred at $L_{r,max} = 1.37$. An increased level of conservatism was observed for FAD with numerical and simplified analytical formulations. For T benchmark specimens the error range went from 2% – 15% to 9% – 27%, for numerical formulations, and from 0% – 16% to 11% – 30%, for simplified analytical formulations. While for B benchmark specimens the error range went from 2% – 18% to 9% – 32%, for numerical formulations, and from 6% – 18% to 6% – 28%, for simplified analytical formulations.

The BS7910 formulation accounts for local yielding and failure at $L_{r,max}$ implies that yield stress is reached at the notch root prior to failure. Consequently, an important stress relaxation is expected, as shown by numerical simulations performed for fatigue specimens at high load levels in [63]. Therefore, considering the stress relaxation because of local notch yielding and the conservatism shown by computational CDF analyses (where residual stresses were not considered), the effect of residual stresses (shown in Tables C.4 and C.5 for FAD) was neglected for the other assessment methods.

6. Theory of critical distances analyses

The Theory of Critical Distances (TCD) was employed to estimate the failure loads of all T and B benchmark specimens using the same FE models described in Section 4 but considering only linear elastic material properties. For each model, the Von Mises equivalent stress σ_{VM} was extracted on a 2 mm path starting from each crack tip. When dealing with materials that show a significant development of plastic deformation before failure, such as this AlSi10Mg alloy, material inherent strength σ_0 and critical distance L have to be estimated with dedicated experiments on specimens with blunt and sharp notches [26,27]. Therefore, two different conditions were considered:

1. the stress field ahead of a small crack originating from the root of a semicircular notch, heavily influenced by stress concentration, i.e.: a “Blunt” notch (Specimen T N1 J3 D0.25$_E$ 2).
2. the stress field ahead of a large crack, independent from the stress concentration induced by the notch, i.e.: a “Sharp” notch (Specimen T N2 J1 D2$_P$ 2).

The material inherent strength σ_0 and the critical distance L were estimated from the intersection point ($L/2$, σ_0) between the two stress fields corresponding to the experimental failure loads, as shown in Fig. 13(a). The resulting values were:

- σ_0 = 522 MPa
- L = 0.5458 mm

Fig. 13(a) also shows the stress distributions at failure for all the T benchmark specimens; all curves cross at the ($L/2$, σ_0) point identified by specimens T N1 J3 D0.25 2 and T N2 J1 D2 2. Fig. 13(c) and Fig. 13(d) provide a comparison between the failure loads estimated with the TCD versus the experimental failure loads for T (F_{TCD}) and B (M_{TCD}) specimens, respectively. Failure loads estimated with TCD for T specimens showed very good agreement with the experimental loads, with a maximum error below 5%. Failure loads estimated with TCD for B specimens had a higher error ($\approx$ 10%), on the conservative side. The discrepancy observed for the B specimens can be ascribed to the fact that material parameters L and σ_0 were obtained for T specimens, while the material parameters could be slightly different for B benchmark specimens, as is suggested by the stress distributions at failure for B benchmark specimens reported in Fig. 13(b), which show that all the curves are slightly above the ($L/2$, σ_0) point.

7. Discussion

7.1. Limitations of the investigated prediction methods

As shown in Sections 4–6, computational CDF, FAD and the TCD approach allowed to correctly predict the failure loads within a ±10% error. For computational CDF and FAD, the complexity of the analyses lies in the computational effort required to model elastic–plastic material properties. The FAD with BS7910 analytical computation of F_0 and M_0 provided too conservative failure predictions. Moreover, all the investigated FAD formulations relied heavily on an accurate description of the SIF. On the other hand, TCD predictions were carried out with simple linear elastic simulations but required additional material properties. However, the

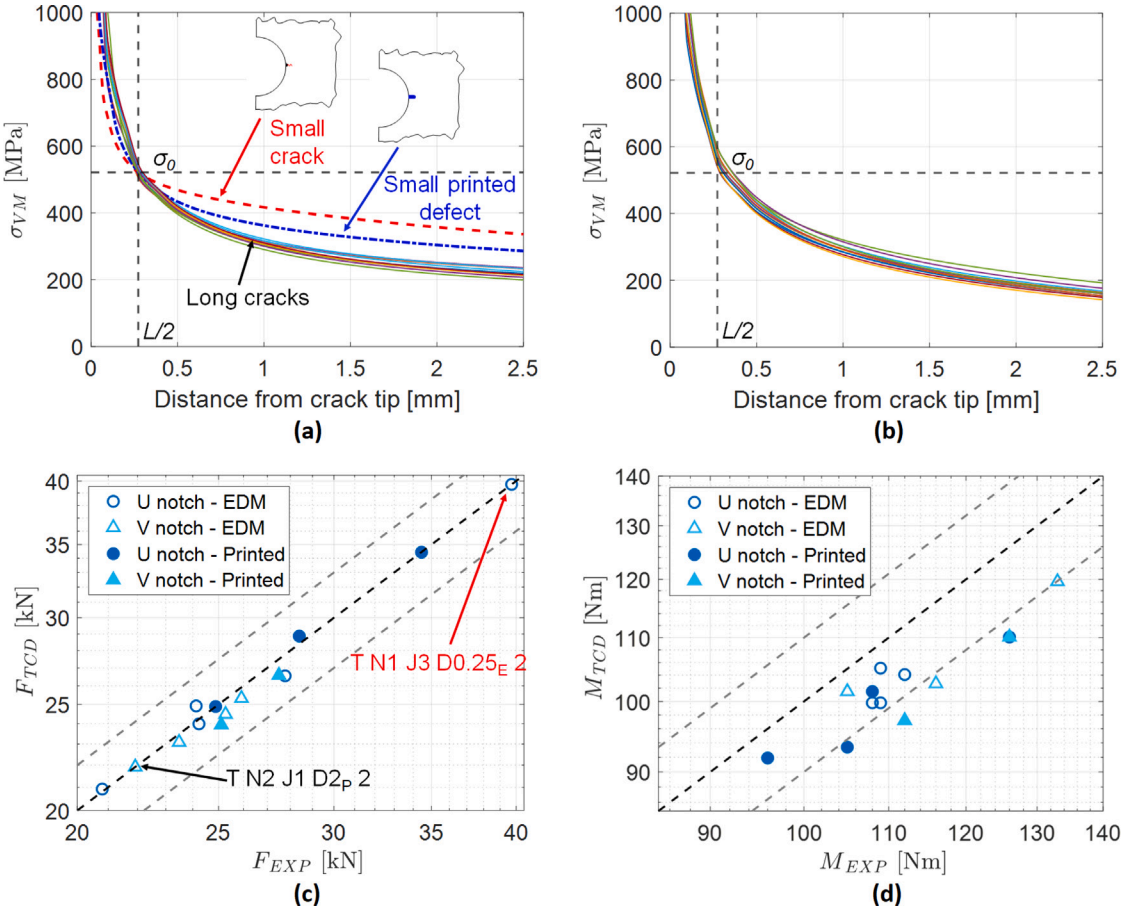

Fig. 13. Theory of Critical Distances analyses for T and B benchmark specimens: (a) Von Mises equivalent stress field ahead of the crack tip for T benchmark specimens, highlighting the curves for a small crack originating from the root of a semicircular notch and a small printed defect. The intersection point represents the material parameter σ_0 and one half of the critical distance L, calibrated on specimens T N1 J3 D0.25$_E$ 2 and T N2 J1 D2$_P$ 2; (b) Von Mises equivalent stress field ahead of the crack tip for B benchmark specimens; comparison of predicted failure loads with the TCD approach versus experimental failure loads for: (c) T benchmark specimens and (d) B benchmark specimens.

main limitation that arised for all of the investigated methods was the required explicit modelling of a crack in the component. From a static assessment point of view, this translates into the necessity of carrying out several FE analyses with different cracked models, one for each critical crack location and orientation with respect to the applied load. Such a procedure to determine critical flaw size, for components that contain several stress raisers as in Additive Manufacturing (AM) topology optimized aerospace parts [2], is then unfeasible.

7.2. Analytical approximation of EPFM via an imaginary crack method

To overcome the limitations of the discussed computational approaches, the authors investigated the possibility to apply an ICM. Hu and Liang [36] proposed an approximation of EPFM via an ICM approach, which allows to determine the critical load for metallic components.

The formulation for the simple case of a large plate with an edge crack of length a subjected to a remote tensile stress σ is:

$$\sigma = R_{p,0.2\%} \cdot \sqrt{\frac{a^*_\infty}{a + a^*_\infty}} \tag{11}$$

The model links two different types of failure, unstable crack propagation and plastic collapse, using the imaginary crack length a^*_∞ which is defined as:

$$a^*_\infty = \frac{1}{\pi} \cdot \left(\frac{K_{I,c}}{Y \cdot R_{p,0.2\%}} \right)^2 \tag{12}$$

where the boundary correction factor Y is equal to 1.12 for the considered case. In fact, for small crack lengths ($a \ll a^*_\infty$) the critical condition is the plastic collapse of the net section and $\sigma \rightarrow R_{p,0.2\%}$, while for large crack lengths ($a \gg a^*_\infty$) the critical condition

is fracture instability and $\sigma \rightarrow \frac{K_{I,c}}{Y \cdot \sqrt{\pi \cdot a}}$, which is the expression of the critical remote stress from LEFM. Finally, for values of crack length a comparable with a^*_∞, Eq. (11) provides an approximation of EPFM. The use of a Fictitious Crack Length (FCL) method to approximate EPFM for static loads, similar to the one proposed by Hu and Liang, has been investigated by the authors. In the following, we derive the analytical formulations employed to estimate the critical load of notched components using the analysed T and B benchmark specimens. The limit condition for the non-cracked component can be identified as the collapse load, which is the load for which the ligament reaches the flow stress, neglecting the presence of the notch: F_{flow} for T specimens and M_{flow} for B specimens. F_{flow} is simply computed as $F_{flow} = \sigma_{flow} \cdot W \cdot B$, assuming a constant stress on the net section as in Fig. 14(a). On the other hand, M_{flow} is obtained as the moment of plastic collapse of the net section at flow stress, with a stress distribution shown in Fig. 14(b). For rectangular sections, this moment corresponds to 1.5 time the moment of first yielding $M^*_{I,p}$ using flow stress instead of yield strength, thus obtaining $M_{flow} = \frac{1.5 \cdot \sigma_{flow} \cdot W^2 \cdot B}{6}$. The next step is to consider how the collapse load changes when the resistant section is decreased by the presence of a crack. In fact, with increasing crack length the collapse load decreases linearly for tensile loads while the decrease is parabolic for bending:

$$F_{flow,crack} = F_{flow} \cdot \left(1 - \frac{a}{W}\right) = \left(\sigma_{flow} \cdot W \cdot B\right) \cdot \left(1 - \frac{a}{W}\right) \tag{13}$$

$$M_{flow,crack} = M_{flow} \cdot \left(1 - \frac{a}{W}\right)^2 = \left(\frac{1.5 \cdot \sigma_{flow} \cdot W^2 \cdot B}{6}\right) \cdot \left(1 - \frac{a}{W}\right)^2 \tag{14}$$

The second limit condition to account for is fracture instability and is given by LEFM. Considering that the limit stress is σ_{flow}, rather than $R_{p,0.2\%}$, the FCL a_0 has to be rewritten as:

$$a_0 = \frac{1}{\pi} \cdot \left(\frac{K_{I,c}}{Y \cdot \sigma_{flow}}\right)^2 \tag{15}$$

where a boundary correction factor $Y = 1.12$ can be assumed for both T and B specimens. From a theoretical point of view, Y should depend on a/W but this assumption well approximates the true boundary correction for the investigated geometries up to significant crack lengths (i.e. $a/W \leq 0.4$) [67].

The critical loads F_{crit} and M_{crit} can then be obtained simply by multiplying the collapse loads for the cracked components by the correction factor $\sqrt{\frac{a_0}{a+a_0}}$, finally obtaining the equations for the proposed FCL model:

$$F_{crit} = F_{flow} \cdot \left(1 - \frac{a}{W}\right) \cdot \sqrt{\frac{a_0}{a + a_0}} \tag{16}$$

$$M_{crit} = M_{flow} \cdot \left(1 - \frac{a}{W}\right)^2 \cdot \sqrt{\frac{a_0}{a + a_0}} \tag{17}$$

Fig. 14(c) and (d) show the critical loads F_{crit} and M_{crit} for T and B benchmark specimens, respectively. The critical loads are normalized by the load of first yield of the net non-cracked section without considering the presence of the notch, F^*_y for T benchmark specimens and $M^*_{I,p}$ for B benchmark specimens. The comparison between the failure loads estimated with the FCL method and the experimental failure loads for T (F_{FCL}) and B (M_{FCL}) benchmark specimens is provided respectively in Fig. 14(e) and (f).

The predictions obtained with the FCL formulation are very close to the experimental failures, with a maximum error within ±10% for T and B benchmark specimens.

7.2.1. FCL formulation for B3D specimens

Following the promising results obtained on T and B benchmark specimens, the authors investigated the possibility to extend the FCL methodology to B3D specimens using the same formulation for B specimens and an equivalent 2D defect depth a_{eq} for the semielliptical defects:

$$a_{eq} = \frac{area}{B} \tag{18}$$

The area of the defect ($area = \frac{\pi \cdot a \cdot c}{2}$) is divided by the thickness B in order to account for the reduction of load carrying capability of the specimen close to the peak stress at the notch (Fig. 14(b)). As for the T and B benchmark specimens, the resulting failure bending moment predictions were close to the experimental values, with a maximum error < ±10%, as shown in Fig. 15 and reported in Table C.3 in Appendix C.

Table 4 provides a comparison between FCL and the other investigated methods in terms of complexity of the FE analyses, required material properties and prediction accuracy. The accuracy is expressed considering the minimum and maximum values of the prediction error $(P_{EXP} - P_{prediction})/P_{EXP}$. It is important to underline that the accuracy of FAD approaches depends strongly on the accuracy of the SIF solutions.

From the point of view of the practical applications, FCL does not require any detailed FE analyses of the cracked component nor any additional material parameters other than yield strength, ultimate tensile stress and fracture toughness. Moreover, FCL formulations allow to directly draw Limit Load Diagrams, representing critical crack size versus applied load, as shown in Fig. 14(c,d) and Fig. 15(a). Using Limit Load Diagrams, it is simple to account for the safety factors required by NASA [68,69] and ESA [70] for the determination of acceptable flaw size, as previously demonstrated by the authors in [11]. Therefore, it can be said that this method is an interesting simplification for determining the acceptable flaw size of notched components under static loads. Finally,

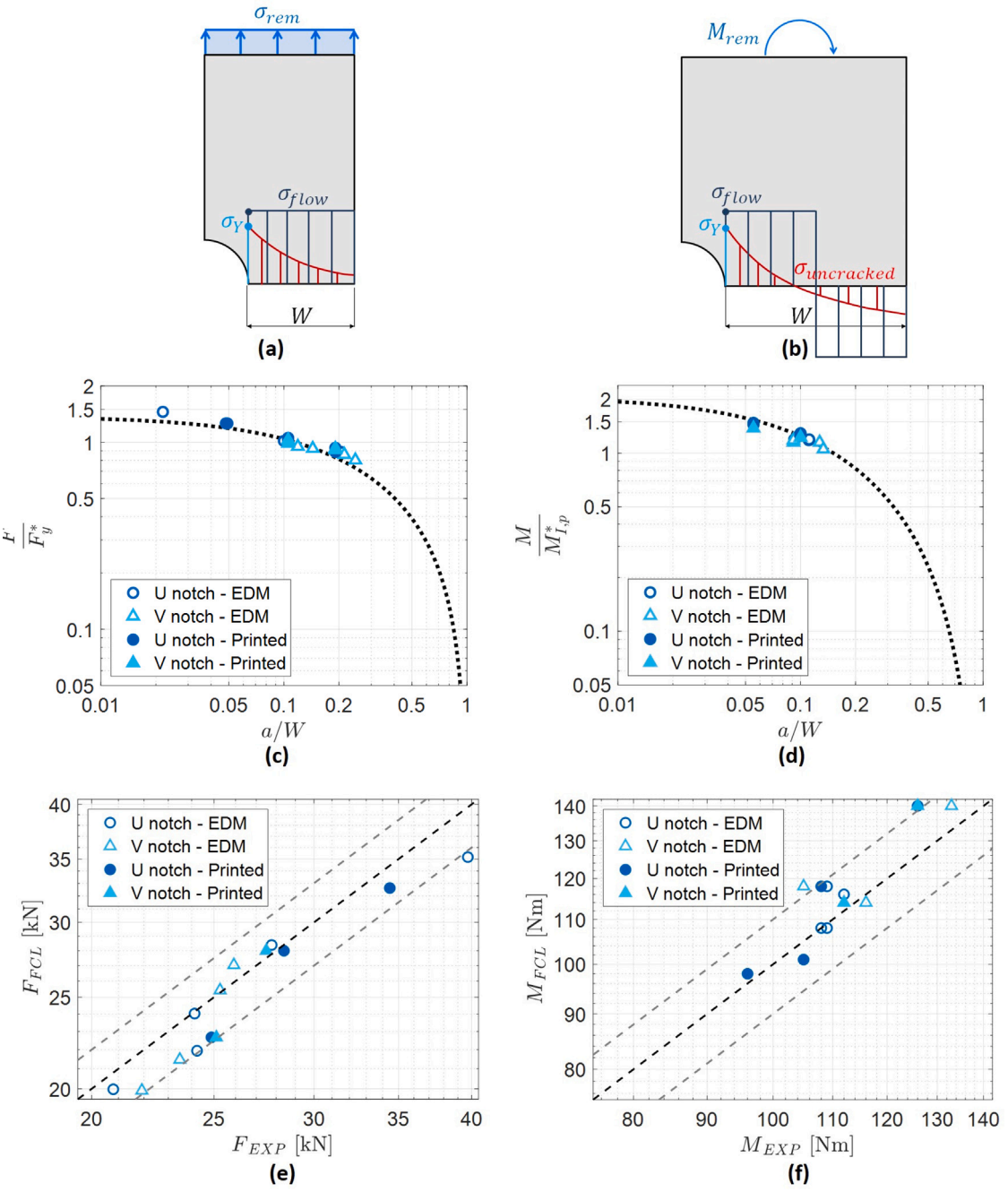

Fig. 14. Fictitious Crack Length analyses for T and B benchmark specimens: schemes for the computation of F_{flow} and M_{flow} for (a) Tensile and (b) Bending benchmark specimens; Limit Load Diagrams for (c) Tensile and (d) Bending specimens; comparison of predicted failure loads with the FCL approach versus experimental failure loads for (e) T benchmark specimens and (f) B benchmark specimens.

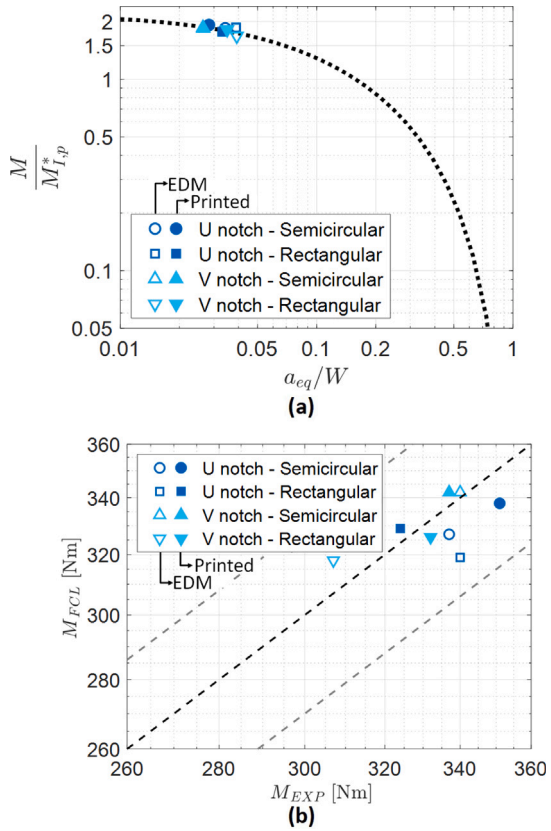

Fig. 15. Fictitious Crack Length analyses for B3D benchmark specimens: (a) Limit Load Diagrams and (b) comparison of predicted failure loads.

Table 4
Comparison between the investigated static assessment methodologies.

Method		FE analysis	Material properties	Accuracy (Error range)
CDF		Cracked component Elastic–Plastic analysis	Stress–strain curve $J_{I,c}$	Very good (0% to 17%)
FAD	Numerical	Cracked component Elastic–Plastic analysis	Stress–strain curve $K_{I,c}$	Very good (2% to 17%)
	BS7910	Non-cracked component Linear elastic analysis	Stress–strain curve $K_{I,c}$	Poor (23% to 45%)
	Simplified	Non-cracked component Linear elastic analysis	Stress–strain curve $K_{I,c}$	Very good (0% to 18%)
TCD		Cracked component Linear elastic analysis	Ad-hoc calibration tests $K_{I,c}$	Excellent (−3% to 13%)
FCL		Non-cracked component Linear elastic analysis	$R_{p,0.2\%}$ and UTS $K_{I,c}$	Good (−12% to 10%)

it is to be noted that, for loading conditions or geometries more complex than the ones examined in this work, the definition of the plastic collapse condition may not be straightforward. For such cases, it would be interesting to investigate the use of a reference stress, similar to the one employed by FAD, to define the plastic collapse condition.

8. Conclusions

This paper considers the static assessment of notched AlSi10Mg components manufactured by L-PBF. In the first part, static fracture tests were performed on three benchmark geometries representing typical AM components: thin notched plates loaded

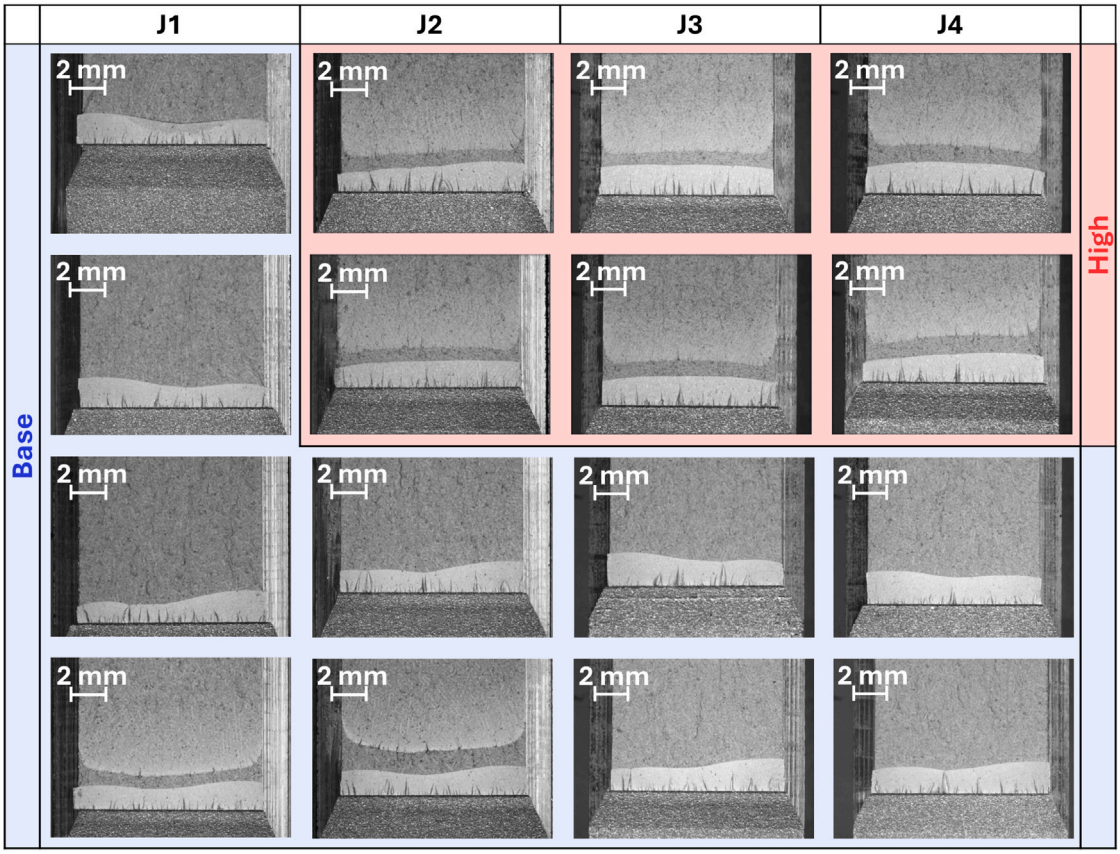

Fig. A.1. Fractographies of CT specimens for build jobs J1 to J4.

in tension or bending and thick notched components subjected to bending. In the second part of the work, the experimental results obtained on the benchmark specimens were compared with numerical predictions using the CDF approach. Fractures of thin benchmark specimens were also investigated with the FAD and the TCD methods. Finally, a new simplified approach, which does not involve any FE modelling of cracked components, was proposed.

The following conclusions can be drawn:

- Material properties obtained on specimens in the AB condition (i.e. without heat treatments) are affected by the different thermal history along the building direction. It is important to consider the proper material condition in order to obtain accurate estimates of the failure loads.
- Failure loads of specimens with manufacturing flaws are notably close to the failure loads of cracked specimens.
- The static assessment of benchmark specimens based on the elastic–plastic fracture mechanics parameter's J-integral obtained with numerical simulations provides good estimates of the fracture behaviour, with a maximum error of 17%, confirming that an elastic–plastic approach is needed even for this AlSi10Mg alloy with quasi-brittle behaviour.
- Computational methods such as FAD and TCD provide very good estimates of the failure load of Tensile and Bending benchmark specimens, with maximum errors of 17% for FAD and 13% for TCD. However, they all require explicit FE modelling of the cracked component.
- The newly proposed FCL method, obtained by modifying an ICM model, provides good approximation of the failure loads for the Tensile, Bending and Bending with three-dimensional defects benchmark specimens using only analytical formulations, with a maximum error of 12%. The FCL method provides an interesting simplification for determining the acceptable flaw size for notched components under static loads. However, more work needs to be done to extend it for more complex loading conditions and geometries.

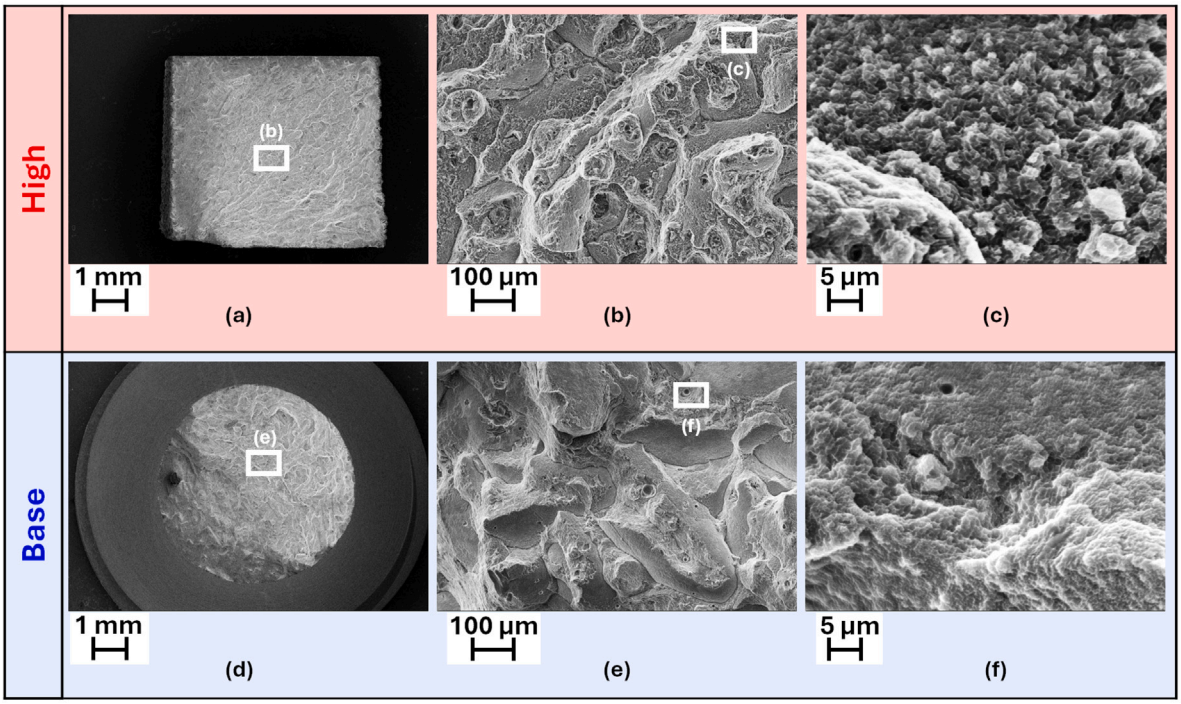

Fig. A.2. Fractographies of one Base and one High tensile specimens from build job J2 obtained with the SEM at (a,d) 40x, (b,e) 500x and (c,f) 7000x magnifications.

CRediT authorship contribution statement

G. Minerva: Writing – review & editing, Writing – original draft, Visualization, Methodology, Investigation, Conceptualization. **I. Pozzoni:** Writing – original draft, Investigation, Data curation. **F. Zarei:** Writing – original draft, Investigation, Data curation. **S. Beretta:** Writing – review & editing, Supervision, Project administration, Funding acquisition, Conceptualization.

Declaration of competing interest

The authors declare the following financial interests/personal relationships which may be considered as potential competing interests: S. Beretta reports financial support was provided by European Space Agency. If there are other authors, they declare that they have no known competing financial interests or personal relationships that could have appeared to influence the work reported in this paper.

Data availability

Data will be made available on request.

Acknowledgements

The authors would like to acknowledge the Italian Ministry of Education, University and Research for the support provided through the Project "Department of Excellence LIS4.0 - Lightweight and Smart Structures for Industry 4.0". The present work was supported by ESA's "IAMSPACE – Italy for Additive Manufacturing in SPACE" project, contract number 4000129932/20/NL/AR. The authors would also like to acknowledge Leonardo S.p.a., especially Mr. Romano Giovanni Iazurlo and Mr. Emanuele Capuano, for permission to publish the results of material characterization tests in SR conditions obtained within the research contract 164/21CR between Leonardo S.p.a. and Politecnico di Milano.

Appendix A. Fractographies of standard specimens

Fractographies of CT specimens for build jobs J1 to J4 obtained with an AxioVision optical stereo microscope showing notch, pre-cracking, stable propagation (test) and unstable propagation regions are reported in Fig. A.1. For specimens that did not fail for unstable propagation during the test, the stable propagation was marked by fatigue cycling, as suggested by ASTM E1820 [40].

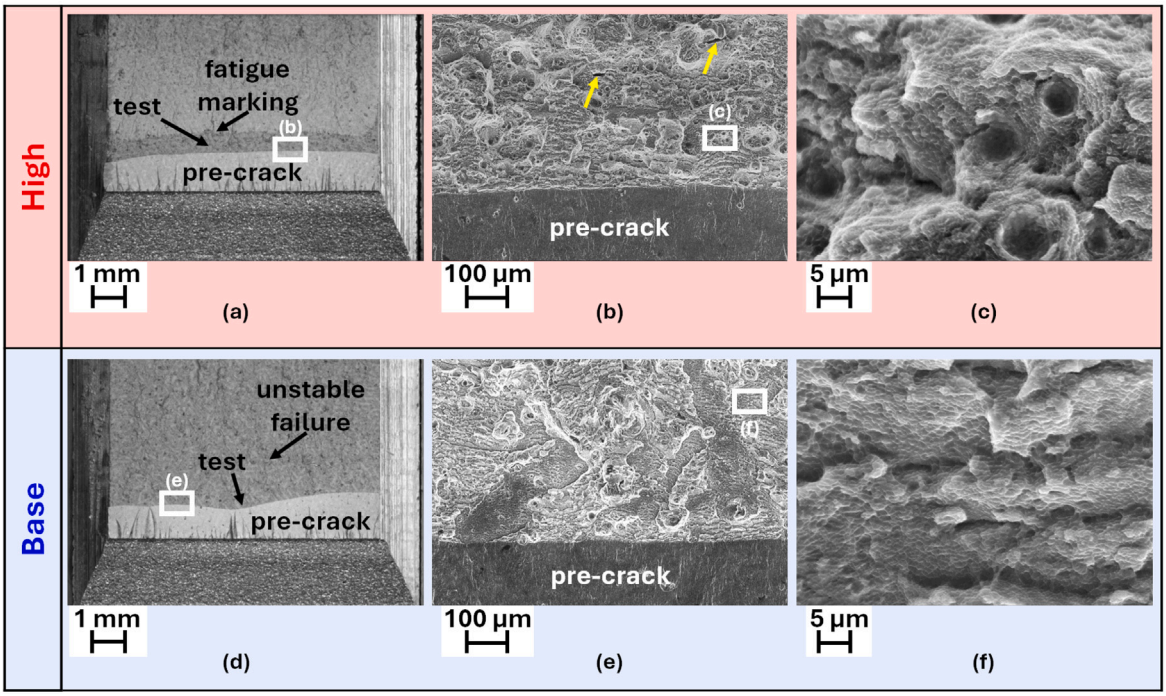

Fig. A.3. Fractographies of one Base and one High CT specimens from build job J2 obtained with the optical stereomicroscope (a,c) and with the SEM at (a,d) 40x, (b,e) 500x and (c,f) 7000x magnifications. Yellow arrows highlight secondary cracks in the High CT specimen.

Table B.1
Average crack sizes, specimen thickness, remote width and width at the notch root for Tensile benchmark specimens.

Specimen	a_{dx} [mm]	a_{xx} [mm]	B [mm]	W_{rem} [mm]	W [mm]
T N1 J1 $D1_E$ 1	0.57	2.02	5.65	39.07	16.9
T N1 J1 $D2_E$ 1	0.56	1.24	5.59	39.12	18.1
T N1 J1 $D2_E$ 2	2.03	2.48	5.69	38.9	22
T N1 J3 $D0.25_E$ 1	0.57	1.62	5.72	38.84	22
T N1 J3 $D0.25_E$ 2	0.26	0.21	5.71	39.1	22
T N1 J2 $D1_P$ 1	1.16	1.16	5.68	39.02	22
T N1 J2 $D1_P$ 2	1.16	1.16	5.71	38.97	22
T N1 J2 $D2_P$ 1	2.1	2.1	5.69	38.87	22
T N1 J2 $D2_P$ 2	2.1	2.1	5.68	39.05	22
T N1 J3 $D0.5_P$ 1	0.54	0.54	5.7	39.01	22
T N1 J3 $D0.5_P$ 2	0.54	0.54	5.72	39.11	22
T N2 J1 $D1_E$ 1	1.05	1.58	5.48	38.95	22
T N2 J1 $D1_E$ 2	1.22	1.93	5.58	39.12	22
T N2 J1 $D2_E$ 1	2.09	2.62	5.63	38.62	22
T N2 J1 $D2_E$ 2	2.25	3.15	5.62	39.13	22
T N2 J2 $D1_P$ 1	1.16	1.16	5.7	38.82	22
T N2 J2 $D1_P$ 2	1.16	1.16	5.68	38.8	22
T N2 J2 $D2_P$ 1	2.1	2.1	5.71	38.79	22
T N2 J2 $D2_P$ 2	2.1	2.1	5.69	38.83	22

Appendix B. Fracture surface measurements

See Tables B.1–B.3.

Appendix C. Failure predictions

See Tables C.1–C.5.

Table B.2
Average crack size, specimen thickness, remote width and width at the notch root for Bending benchmark specimens.

Specimen	a [mm]	B [mm]	W_{rem} [mm]	W [mm]
B N1 J1 $D1_E$ 1	1.94	5.67	29.93	21
B N1 J1 $D1_E$ 2	2	5.68	29.94	21
B N1 J1 $D2_E$ 1	2.33	5.69	30.05	21
B N1 J1 $D2_E$ 2	2.34	5.69	29.58	21
B N1 J2 $D1_P$ 1	1.16	5.68	28.76	21
B N1 J2 $D1_P$ 2	1.16	5.67	28.83	21
B N1 J2 $D2_P$ 1	2.1	5.7	28.77	21
B N1 J2 $D2_P$ 2	2.1	5.69	28.81	21
B N2 J1 $D1_E$ 1	1.92	5.7	29.23	21
B N2 J1 $D1_E$ 2	1.92	5.68	30.05	21
B N2 J1 $D2_E$ 1	2.67	5.7	30.12	21
B N2 J1 $D2_E$ 2	2.8	5.67	29.58	21
B N2 J2 $D1_P$ 1	1.16	5.7	28.81	21
B N2 J2 $D2_P$ 1	2.1	5.68	28.73	21

Table B.3
Average crack depth and half width, specimen thickness, remote width and width at the notch root for Bending benchmark specimens with 3D defects.

Specimen	a [mm]	c [mm]	B [mm]	W_{rem} [mm]	W [mm]
B3D N1 J4 DS_E	1.86	2.93	11.85	30.05	21
B3D N1 J4 DR_E	1.39	4.43	11.88	30.03	21
B3D N1 J4 DS_P	2.14	2.12	11.88	29.96	21
B3D N1 J4 DR_P	1	4.18	11.93	29.98	21
B3D N2 J4 DS_E	1.94	2.18	11.82	30.15	21
B3D N2 J4 DR_E	1.35	4.59	11.88	29.98	21
B3D N2 J4 DS_P	2.02	2.11	11.86	30	21
B3D N2 J4 DR_P	1.05	4.13	11.92	29.96	21

Table C.1
Comparison between failure loads predicted with different methods and experimental failure loads for notched Tensile specimens.

Specimen	F_{fail} [N]					
	FAD			TCD	FCL	Experimental
	Numerical	BS7910	Simplified			
T N1 J1 $D1_E$ 1	19 554	14 665	19 477	20 921	23 026	20 804
T N1 J1 $D2_E$ 1	22 938	17 470	22 809	24 922	26 827	24 130
T N1 J1 $D2_E$ 2	22 887	17 745	23 344	23 998	24 581	24 237
T N1 J3 $D0.25_E$ 1	25 275	19 614	25 411	26 551	30 175	27 770
T N1 J3 $D0.25_E$ 2	34 051	22 679	33 341	39 718	38 293	39 718
T N1 J2 $D1_P$ 1	26 958	20 614	27 206	28 866	29 783	28 825
T N1 J2 $D1_P$ 2	26 958	20 614	27 206	28 866	29 783	28 035
T N1 J2 $D2_P$ 1	23 666	18 571	24 156	24 890	25 139	24 266
T N1 J2 $D2_P$ 2	23 666	18 571	24 156	24 890	25 139	25 501
T N1 J3 $D0.5_P$ 1	31 328	21 962	31 081	34 431	34 769	34 447
T N1 J3 $D0.5_P$ 2	31 328	21 962	31 081	34 431	34 871	34 458
T N2 J1 $D1_E$ 1	24 374	15 565	24 301	25 322	25 406	25 920
T N2 J1 $D1_E$ 2	23 646	14 942	23 614	24 487	24 398	25 277
T N2 J1 $D2_E$ 1	22 278	13 715	22 497	23 087	22 072	23 489
T N2 J1 $D2_E$ 2	21 499	12 773	21 762	21 917	21 214	21 917
T N2 J2 $D1_P$ 1	25 358	16 313	25 337	26 584	26 023	28 078
T N2 J2 $D1_P$ 2	25 358	16 313	25 337	26 584	26 023	26 917
T N2 J2 $D2_P$ 1	23 055	14 640	23 303	23 954	22 753	25 294
T N2 J2 $D2_P$ 2	23 055	14 640	23 303	23 954	22 753	24 920

Table C.2
Comparison between failure bending moments predicted with different methods and experimental failure bending moments for notched Bending specimens.

Specimen	M_{fail} [N m]					
	FAD			TCD	FCL	Experimental
	Numerical	BS7910	Simplified			
B N1 J1 $D1_E$ 1	106	77	102	105	118	109
B N1 J1 $D1_E$ 2	105	77	101	104	116	112
B N1 J1 $D2_E$ 1	101	74	97	100	108	108
B N1 J1 $D2_E$ 2	101	74	97	100	108	109
B N1 J2 $D1_P$ 1	120	84	116	120	140	133
B N1 J2 $D1_P$ 2	120	84	116	120	140	135
B N1 J2 $D2_P$ 1	104	76	100	103	114	116
B N1 J2 $D2_P$ 2	104	76	100	103	114	118
B N2 J1 $D1_E$ 1	103	66	99	102	118	105
B N2 J1 $D1_E$ 2	103	66	99	102	118	108
B N2 J1 $D2_E$ 1	95	63	91	93	101	105
B N2 J1 $D2_E$ 2	94	63	90	92	98	96
B N2 J2 $D1_P$ 1	104	69	103	110	140	126
B N2 J2 $D2_P$ 1	101	65	97	97	114	112

Table C.3
Comparison between failure bending moments predicted with different methods and experimental failure bending moments for notched Bending specimens with 3D defects.

Specimen	M_{fail} [N m]		
	CDF	FCL	Experimental
B3D N1 J4 DS_E	321	327	337
B3D N1 J4 DR_E	306	319	340
B3D N1 J4 DS_P	349	338	351
B3D N1 J4 DR_P	315	329	324
B3D N2 J4 DS_E	335	342	340
B3D N2 J4 DR_E	287	318	307
B3D N2 J4 DS_P	337	342	337
B3D N2 J4 DR_P	288	326	332

Table C.4
Comparison between failure loads predicted with FAD with and without residual stresses for notched Tensile specimens.

Specimen	$F_{fail,FAD}$ [N]					
	Numerical		BS7910		Simplified	
	Without RS	With RS	Without RS	With RS	Without RS	With RS
T N1 J1 $D1_E$ 1	19 554	16 158	14 665	14 665	19 477	15 499
T N1 J1 $D2_E$ 1	22 938	18 421	17 470	17 470	22 809	17 646
T N1 J1 $D2_E$ 2	22 887	20 785	17 745	17 745	23 344	20 431
T N1 J3 $D0.25_E$ 1	25 275	20 160	19 614	19 614	25 411	19 521
T N1 J3 $D0.25_E$ 2	33 708	31 537	22 679	22 679	33 341	31 204
T N1 J2 $D1_P$ 1	26 958	21 593	20 614	20 614	27 206	21 011
T N1 J2 $D1_P$ 2	26 958	21 593	20 614	20 614	27 206	21 011
T N1 J2 $D2_P$ 1	23 666	21 301	18 571	18 571	24 156	20 962
T N1 J2 $D2_P$ 2	23 666	21 301	18 571	18 571	24 156	20 962
T N1 J3 $D0.5_P$ 1	31 328	27 067	21 962	21 962	31 081	26 028
T N1 J3 $D0.5_P$ 2	31 328	27 067	21 962	21 962	31 081	26 028
T N2 J1 $D1_E$ 1	24 374	20 712	15 565	15 565	24 301	19 880
T N2 J1 $D1_E$ 2	23 646	20 743	14 942	14 942	23 614	19 946
T N2 J1 $D2_E$ 1	22 278	20 411	13 715	13 715	22 497	19 853
T N2 J1 $D2_E$ 2	21 499	19 925	12 773	12 773	21 762	19 425
T N2 J2 $D1_P$ 1	25 358	20 910	16 313	16 313	25 337	20 118
T N2 J2 $D1_P$ 2	25 358	20 910	16 313	16 313	25 337	20 118
T N2 J2 $D2_P$ 1	23 055	20 891	14 640	14 640	23 303	20 343
T N2 J2 $D2_P$ 2	23 055	20 891	14 640	14 640	23 303	20 343

Table C.5
Comparison between failure bending moments predicted with FAD with and without residual stresses for notched Bending specimens.

Specimen	$M_{fail,FAD}$ [N m]					
	Numerical		BS7910		Simplified	
	Without RS	With RS	Without RS	With RS	Without RS	With RS
B N1 J1 $D1_E$ 1	106	95	77	77	102	99
B N1 J1 $D1_E$ 2	105	94	77	77	101	98
B N1 J1 $D2_E$ 1	101	92	74	74	97	96
B N1 J1 $D2_E$ 2	101	92	74	74	97	96
B N1 J2 $D1_P$ 1	120	96	84	84	116	101
B N1 J2 $D1_P$ 2	120	96	84	84	116	101
B N1 J2 $D2_P$ 1	104	94	76	76	100	98
B N1 J2 $D2_P$ 2	104	94	76	76	100	98
B N2 J1 $D1_E$ 1	103	93	66	66	99	97
B N2 J1 $D1_E$ 2	103	93	66	66	99	97
B N2 J1 $D2_E$ 1	95	88	63	63	91	92
B N2 J1 $D2_E$ 2	94	87	63	63	90	91
B N2 J2 $D1_P$ 1	104	86	69	69	103	90
B N2 J2 $D2_P$ 1	101	92	65	65	97	96

References

[1] Gisario A, Kazarian M, Martina F, Mehrpouya M. Metal additive manufacturing in the commercial aviation industry: A review. J Manuf Syst 2019;53:124–49. http://dx.doi.org/10.1016/j.jmsy.2019.08.005, URL https://linkinghub.elsevier.com/retrieve/pii/S0278612519300731.

[2] Blakey-Milner B, Gradl P, Snedden G, Brooks M, Pitot J, Lopez E, Leary M, Berto F, du Plessis A. Metal additive manufacturing in aerospace: A review. Mater Des 2021;209:110008. http://dx.doi.org/10.1016/j.matdes.2021.110008, URL https://linkinghub.elsevier.com/retrieve/pii/S0264127521005633.

[3] Qiu C, Panwisawas C, Ward M, Basoalto HC, Brooks JW, Attallah MM. On the role of melt flow into the surface structure and porosity development during selective laser melting. Acta Mater 2015;96:72–9. http://dx.doi.org/10.1016/j.actamat.2015.06.004, URL https://linkinghub.elsevier.com/retrieve/pii/S1359645415003870.

[4] Zhao C, Fezzaa K, Cunningham RW, Wen H, De Carlo F, Chen L, Rollett AD, Sun T. Real-time monitoring of laser powder bed fusion process using high-speed X-ray imaging and diffraction. Sci Rep 2017;7(1):3602. http://dx.doi.org/10.1038/s41598-017-03761-2, URL https://www.nature.com/articles/s41598-017-03761-2.

[5] Leung CLA, Marussi S, Atwood RC, Towrie M, Withers PJ, Lee PD. In situ X-ray imaging of defect and molten pool dynamics in laser additive manufacturing. Nature Commun 2018;9(1):1355. http://dx.doi.org/10.1038/s41467-018-03734-7, URL https://www.nature.com/articles/s41467-018-03734-7.

[6] Zhang J, Song B, Wei Q, Bourell D, Shi Y. A review of selective laser melting of aluminum alloys: Processing, microstructure, property and developing trends. J Mater Sci Technol 2019;35(2):270–84. http://dx.doi.org/10.1016/j.jmst.2018.09.004.

[7] ASTM E3166-20 standard guide for nondestructive examination of metal additively manufactured aerospace parts after build. 2020.

[8] ECSS-E-ST-32-01C Rev.2 - fracture control. Tech. rep., Noordwijk, NL; 2021.

[9] ECSS-Q-ST-70-80C - Space product assurance: Processing and quality assurance requirements for metallic powder bed fusion technologies for space applications. Tech. rep., Noordwijk, NL; 2021.

[10] Zhao L, Song L, Macías JGS, Zhu Y, Huang M, Simar A, Li Z. Review on the correlation between microstructure and mechanical performance for laser powder bed fusion AlSi10Mg. Addit Manuf 2022. http://dx.doi.org/10.1016/j.addma.2022.102914, URL https://linkinghub.elsevier.com/retrieve/pii/S2214860422003116.

[11] Minerva G, Patriarca L, Foletti S, Beretta S. Static assessment of flawed thin AlSi10Mg parts produced by Laser Powder Bed Fusion. Mater Des 2022;224:111292. http://dx.doi.org/10.1016/j.matdes.2022.111292.

[12] Anderson TL. Fracture mechanics: Fundamentals and applications. 3rd ed.. Boca Raton, FL: Taylor & Francis; 2005, p. 610.

[13] Newman Jr JC, Raju IS. Stress-intensity factor equations for cracks in three-dimensional finite bodies subjected to tension and bending loads. In: Atluri SN, editor. Computational methods in the mechanics of fracture. Elsevier Science Publishers; 1986, p. 311–34.

[14] Tada H, Paris PC, Irwin GR. The stress analysis of cracks handbook. 3rd ed.. New York: ASME Press; 2000, p. 677.

[15] BS 7910: Guide to methods for assessing the acceptability of flaws in metallic structures. 2019.

[16] Shih CF, Hutchinson JW. Fully plastic solutions and large scale yielding estimates for plane stress crack problems. J Eng Mater Technol 1976;98(4):289–95. http://dx.doi.org/10.1115/1.3443380.

[17] Zerbst U, Schwalbe K-H, Ainsworth R. An overview of failure assessment methods in codes and standards. In: Comprehensive structural integrity. Elsevier; 2003, p. 1–48. http://dx.doi.org/10.1016/B0-08-043749-4/07053-1.

[18] Hadley I. BS 7910:2013 in brief. Int J Press Vessels Pip 2018;165:263–9. http://dx.doi.org/10.1016/j.ijpvp.2018.07.010.

[19] Zerbst U, Schödel M, Webster S, Ainsworth R. Fitness-for-service fracture assessment of structures containing cracks. Academic Press; 2007, p. 320.

[20] British Energy Generation Ltd. R6 revision 4: Assessment of the integrity of structures containing defects. 2020.

[21] API 579: Recommended practice for fitness for service. 2000.

[22] Iwashita T, Kurobane Y, Azuma K, Makino Y. Prediction of brittle fracture initiating at ends of CJP groove welded joints with defects: study into applicability of failure assessment diagram approach. Eng Struct 2003;25(14):1815–26.

[23] Seifi M, Salem A, Beuth J, Harrysson O, Lewandowski JJ. Overview of materials qualification needs for metal additive manufacturing. Jom 2016;68(3):747–64.

[24] Zerbst U, Bruno G, Buffière J-Y, Wegener T, Niendorf T, Wu T, Zhang X, Kashaev N, Meneghetti G, Hrabe N, Madia M, Werner T, Hilgenberg K, Koukolíková M, Procházka R, Džugan J, Möller B, Beretta S, Evans A, Wagener R, Schnabel K. Damage tolerant design of additively manufactured metallic components subjected to cyclic loading: State of the art and challenges. Prog Mater Sci 2021. http://dx.doi.org/10.1016/j.pmatsci.2021.100786.

[25] Taylor D, Cornetti P, Pugno N. The fracture mechanics of finite crack extension. Eng Fract Mech 2005;72(7):1021–38. http://dx.doi.org/10.1016/j.engfracmech.2004.07.001, URL https://linkinghub.elsevier.com/retrieve/pii/S0013794404001572.

[26] Susmel L, Taylor D. On the use of the theory of critical distances to predict static failures in ductile metallic materials containing different geometrical features. Eng Fract Mech 2008;75(15):4410–21. http://dx.doi.org/10.1016/j.engfracmech.2008.04.018, URL https://linkinghub.elsevier.com/retrieve/pii/S0013794408001082.

[27] Louks R, Askes H, Susmel L. A generalised approach to rapid finite element design of notched materials against static loading using the Theory of Critical Distances. Mater Des 2016;108:769–79. http://dx.doi.org/10.1016/j.matdes.2016.07.047.

[28] Taylor D. The theory of critical distances. Elsevier; 2007, http://dx.doi.org/10.1016/B978-0-08-044478-9.X5000-5, URL https://linkinghub.elsevier.com/retrieve/pii/B9780080444789X50005.

[29] Taylor D. Prediction of fatigue failure location on a component using a critical distance method. Int J Fatigue 2000;22(9):735–42. http://dx.doi.org/10.1016/S0142-1123(00)00062-1, URL https://linkinghub.elsevier.com/retrieve/pii/S0142112300000621.

[30] Crupi G, Crupi V, Guglielmino E, Taylor D. Fatigue assessment of welded joints using critical distance and other methods. Eng Fail Anal 2005;12(1):129–42. http://dx.doi.org/10.1016/j.engfailanal.2004.03.005, URL https://linkinghub.elsevier.com/retrieve/pii/S1350630704000603.

[31] Waddoups M, Eisenmann J, Kaminski B. Macroscopic fracture mechanics of advanced composite materials. J Compos Mater 1971;5(4):446–54. http://dx.doi.org/10.1177/002199837100500402, URL http://journals.sagepub.com/doi/10.1177/002199837100500402.

[32] Barenblatt G. The mathematical theory of equilibrium cracks in brittle fracture. 1962, p. 55–129. http://dx.doi.org/10.1016/S0065-2156(08)70121-2, URL https://linkinghub.elsevier.com/retrieve/pii/S0065215608701212.

[33] Dugdale DS. Yielding of steel sheets containing slits. J Mech Phys Solids 1960;8(2):100–4.

[34] Hillerborg A, Modéer M, Petersson P-E. Analysis of crack formation and crack growth in concrete by means of fracture mechanics and finite elements. Cem Concr Res 1976;6(6):773–81. http://dx.doi.org/10.1016/0008-8846(76)90007-7, URL https://linkinghub.elsevier.com/retrieve/pii/0008884676900077.

[35] Bažant ZP. Scaling theory for quasibrittle structural failure. Proc Natl Acad Sci 2004;101(37):13400–7. http://dx.doi.org/10.1073/pnas.0404096101, URL https://pnas.org/doi/full/10.1073/pnas.0404096101.

[36] Hu X, Liang L. Elastic-plastic and quasi-brittle fracture. In: Handbook of mechanics of materials. Singapore: Springer Singapore; 2018, p. 1–32. http://dx.doi.org/10.1007/978-981-10-6855-3_38-1.

[37] ASTM B215-20 standard practices for sampling metal powders. 2020, http://dx.doi.org/10.1520/B0215-20.

[38] ASTM F3637-23 standard guide for additive manufacturing of metal - finished part properties - methods for relative density measurement. 2023, http://dx.doi.org/10.1520/F3637-23.

[39] ASTM E8/E8M-21 standard test methods for tension testing of metallic materials. 2021, URL https://www.astm.org/Standards/E8.

[40] ASTM E1820-20b standard test method for measurement of fracture toughness. 2020, URL https://www.astm.org/Standards/E1820.

[41] Carboni M, Patriarca L, Regazzi D. Determination of ΔKth by compression pre-cracking in a structural steel. J ASTM Int 2009;6(9):102617. http://dx.doi.org/10.1520/JAI102617, URL http://www.astm.org/doiLink.cgi?JAI102617.

[42] ASTM E92-23 standard test method for vickers hardness and knoop hardness of metallic materials. 2023, http://dx.doi.org/10.1520/E0092-23.

[43] Dowling NE. Mechanical behavior of materials: Engineering methods for deformation, fracture, and fatigue. 4th ed.. Harlow: Pearson; 2013, p. 954.

[44] Buchbinder D, Schleifenbaum H, Heidrich S, Meiners W, Bültmann J. High power selective laser melting (HP SLM) of aluminum parts. Physics Procedia 2011;12:271–8. http://dx.doi.org/10.1016/j.phpro.2011.03.035.

[45] Rosenthal I, Tiferet E, Ganor M, Stern A. Post-processing of AM-SLM AlSi10Mg specimens: Mechanical properties and fracture behaviour. Ann "Dunarea de Jos" Univ Galati Fascicle XII: Weld Equip Technol 2015;26:33–8.

[46] Raus AA, Wahab MS, Ibrahim M, Kamarudin K, Aqeel A, Shamsudin S. Mechanical and physical properties of AlSi10Mg processed through selective laser melting. Int J Eng Technol 2016;8(6):2612–8. http://dx.doi.org/10.21817/ijet/2016/v8i6/160806217.

[47] Hitzler L, Janousch C, Schanz J, Merkel M, Heine B, Mack F, Hall W, Öchsner A. Direction and location dependency of selective laser melted AlSi10Mg specimens. J Mater Process Technol 2017;243:48–61. http://dx.doi.org/10.1016/j.jmatprotec.2016.11.029.

[48] Read N, Wang W, Essa K, Attallah MM. Selective laser melting of AlSi10Mg alloy: Process optimisation and mechanical properties development. Mater Des (1980-2015) 2015;65:417–24. http://dx.doi.org/10.1016/j.matdes.2014.09.044.

[49] Kempen K, Thijs L, Van Humbeeck J, Kruth J-P. Processing AlSi10Mg by selective laser melting: parameter optimisation and material characterisation. Mater Sci Technol 2015;31(8):917–23. http://dx.doi.org/10.1179/1743284714Y.0000000702.

[50] Hitzler L, Schoch N, Heine B, Merkel M, Hall W, Öchsner A. Compressive behaviour of additively manufactured AlSi10Mg. Materwiss Werksttech 2018;49(5):683–8. http://dx.doi.org/10.1002/mawe.201700239.

[51] Liu Q, Wu H, Paul MJ, He P, Peng Z, Gludovatz B, Kruzic JJ, Wang CH, Li X. Machine-learning assisted laser powder bed fusion process optimization for AlSi10Mg: New microstructure description indices and fracture mechanisms. Acta Mater 2020;201:316–28. http://dx.doi.org/10.1016/j.actamat.2020.10.010.

[52] Paul MJ, Liu Q, Best JP, Li X, Kruzic JJ, Ramamurty U, Gludovatz B. Fracture resistance of AlSi10Mg fabricated by laser powder bed fusion. Acta Mater 2021;211. http://dx.doi.org/10.1016/j.actamat.2021.116869.

[53] Araújo LC, Gabriel AH, da Fonseca EB, Avila JA, Jardini AL, Junior RS, Lopes ÉS. Effects of build orientation and heat treatments on the tensile and fracture toughness properties of additively manufactured AlSi10Mg. Int J Mech Sci 2021. http://dx.doi.org/10.1016/j.ijmecsci.2021.106868.

[54] Lupi G, Minerva G, Patriarca L, Casati R, Beretta S. Fracture toughness of AlSi10Mg alloy produced by LPBF: effects of orientation and heat treatment. Int J Fract 2024. http://dx.doi.org/10.1007/s10704-024-00787-2, URL https://link.springer.com/10.1007/s10704-024-00787-2.

[55] Beretta S, Minerva G. Additive manufacturing activities for SHALOM Phase A/B1 Pre-Development - Deliverable 2 technical note 03 - tensile and toughness samples test report. Politecnico di Milano - Dipartimento di Meccanica; 2023.

[56] Li W, Li S, Liu J, Zhang A, Zhou Y, Wei Q, Yan C, Shi Y. Effect of heat treatment on AlSi10Mg alloy fabricated by selective laser melting: Microstructure evolution, mechanical properties and fracture mechanism. Mater Sci Eng A 2016;663:116–25. http://dx.doi.org/10.1016/j.msea.2016.03.088.

[57] Iturrioz A, Gil E, Petite MM, Garciandia F, Mancisidor AM, San Sebastian M. Selective laser melting of AlSi10Mg alloy: influence of heat treatment condition on mechanical properties and microstructure. Weld World 2018;62(4):885–92. http://dx.doi.org/10.1007/s40194-018-0592-8.

[58] Casati R, Hamidi Nasab M, Coduri M, Tirelli V, Vedani M. Effects of platform pre-heating and thermal-treatment strategies on properties of AlSi10Mg alloy processed by selective laser melting. Metals 2018;8(11):954. http://dx.doi.org/10.3390/met8110954.

[59] Cao Y, Lin X, Wang Q, Shi S, Ma L, Kang N, Huang W. Microstructure evolution and mechanical properties at high temperature of selective laser melted AlSi10Mg. J Mater Sci Technol 2021;62:162–72. http://dx.doi.org/10.1016/j.jmst.2020.04.066.

[60] Heilgeist S, Heine B, Merkel M, Hitzler L, Javanbakht Z, Öchsner A. The influence of post-heat treatments on the tensile strength and surface hardness of selectively laser-melted AlSi10Mg. Materwiss Werksttech 2019;50(5):546–52. http://dx.doi.org/10.1002/mawe.201800236.

[61] Zerbst U, Madia M, Kiyak Y, Breidung M, Baer W, Küppers M. Stiffness/constraint effects in analytical flaw assessment. A technical note. Eng Fract Mech 2022;273:108728. http://dx.doi.org/10.1016/j.engfracmech.2022.108728.

[62] Hadley I, Zerbst U, Coules H, James P, Sharples J, Bhat SS, Larrosa N. Knowledge gaps in fitness-for-service assessment procedures; summary of the 2nd 'mind the gap' workshop. Int J Press Vessels Pip 2023;202:104883. http://dx.doi.org/10.1016/j.ijpvp.2022.104883.

[63] Sausto F, Tezzele C, Beretta S. Analysis of fatigue strength of L-PBF AlSi10Mg with different surface post-processes: Effect of residual stresses. Metals 2022;12(6):898. http://dx.doi.org/10.3390/met12060898.

[64] Sausto F, Carrion P, Shamsaei N, Beretta S. Fatigue failure mechanisms for AlSi10Mg manufactured by L-PBF under axial and torsional loads: The role of defects and residual stresses. Int J Fatigue 2022;162:106903. http://dx.doi.org/10.1016/j.ijfatigue.2022.106903, URL https://linkinghub.elsevier.com/retrieve/pii/S0142112322001736.

[65] Beretta S, Patriarca L, Gargourimotlagh M, Hardaker A, Brackett D, Salimian M, Gumpinger J, Ghidini T. A benchmark activity on the fatigue life assessment of AlSi10Mg components manufactured by L-PBF. Mater Des 2022;218:110713. http://dx.doi.org/10.1016/j.matdes.2022.110713, URL https://linkinghub.elsevier.com/retrieve/pii/S0264127522003355.

[66] Lehner P, Blinn B, Zhu T, Al-Zuhairi A, Smaga M, Teutsch R, Beck T. Influence of the as-built surface and a T6 heat treatment on the fatigue behavior of additively manufactured AlSi10Mg. Int J Fatigue 2024;187:108479. http://dx.doi.org/10.1016/j.ijfatigue.2024.108479.
[67] Hammond MJ, Fawaz SA. Stress intensity factors of various size single edge-cracked tension specimens: A review and new solutions. Eng Fract Mech 2016;153:25–34. http://dx.doi.org/10.1016/j.engfracmech.2015.12.022, URL https://linkinghub.elsevier.com/retrieve/pii/S0013794415006980.
[68] NASA. NASA-STD-5001B structural design and test factors of safety for spaceflight hardware. 2014.
[69] McElroy. A summary of NASA-HDBK-5026: Guidance on strength, fatigue, and fracture control requirements for additive manufactured spaceflight hardware. 2021, p. 39, Presentation at ICAM 2021, available at: https://ntrs.nasa.gov/citations/20210020710.
[70] ECSS-E-ST-32-10C Rev.2 - Structural factors of safety for spaceflight hardware. Tech. rep., Noordwijk, NL; 2019.